GraphGas: Optimizing Outlet of Microcolumns for Gas Chromatography

Kaitlin Howell, Section Microtechnique

Assistant: *Ulrike Lehmann*

Professeur: *Guillermo Villanueva*

This master thesis focused on optimizing the outlet geometry of microcolumn chips and how the chips are assembled in a miniaturized gas analysis system based on the principles of gas chromatography. The theory and literature of gas chromatography at microscales was studied and consequently several outlet designs were simulated with COMSOL Multiphysics®. Their theoretical velocity profiles were calculated at multiple positions in reference to a geometry acting as an gas sensor within the simulation models.

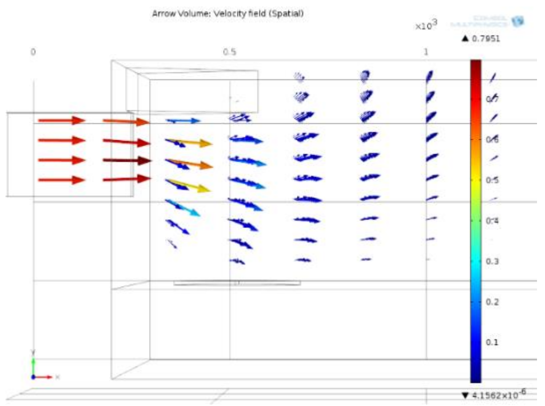

Example FEA results for a side outlet design

The five most promising outlet geometry designs were in CMi at EPFL. Two process flows were used during the fabrication phase, the second including steps for creating structures of SU8 surrounding the outlets to act as nozzles.

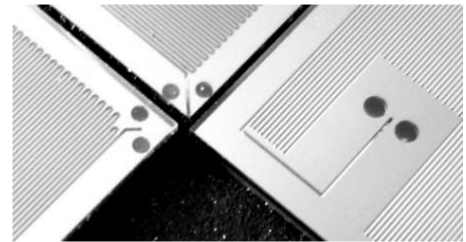

Three outlet designs fabricated in CMi

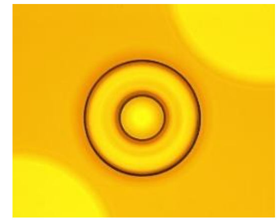

SU8 nozzle surrounding an microcolumn outlet

Five different outlets geometries were fabricated and four outlets were tested at various positions above a metal oxide sensor to see the influence of the fluid velocity near the sensor on the peak height and full width at half maximum of the output peaks for sample volume with one analyte.

The experimental results show that there is a correlation between the velocity and measured peak height, but the full width half maximum is controlled by other aspects of the microcolumn.

GraphGas
Optimizing Outlets of Microcolumns for Gas Chromatography

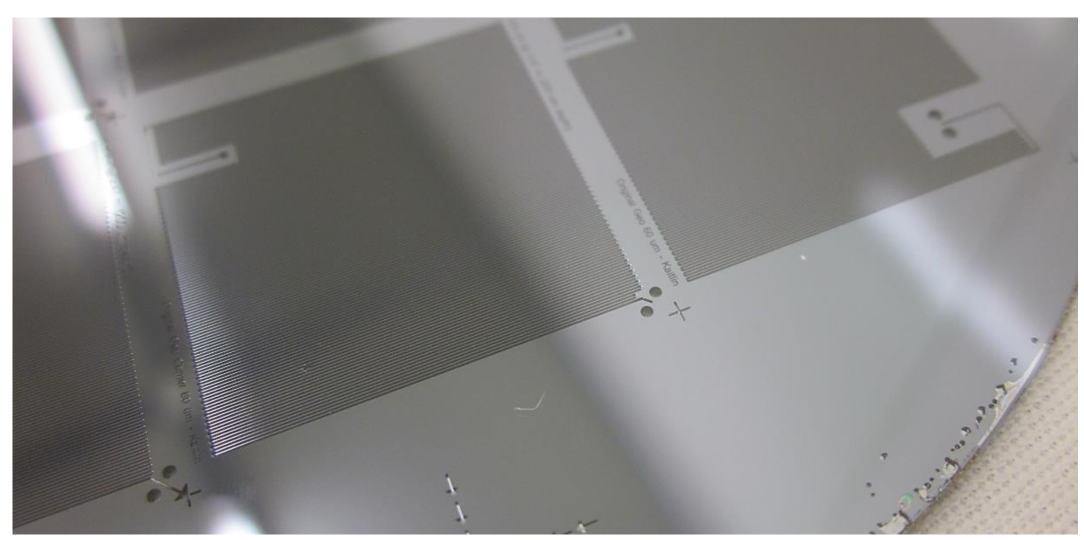

Master Thesis

Student: Kaitlin Howell
Professor: Guillermo Villanueva
Supervisor: Ulrike Lehmann

Table of Contents

Acknowledgements 5
1. Introduction 6
2. Theory 8
  2.1 Gas Chromatography 8
  2.2 Fluid Dynamics 11
3. Finite Element Analysis 12
  3.1 1st Simulation Run 15
  3.2 2nd Simulation Run 16
  3.3 3rd Simulation Run 21
  3.4 Discussion 25
4. Fabrication 26
  4.1 Mask Design 27
  4.2 Photolithography 30
  4.3 Etching 31
  4.4 SU8 Nozzle Fabrication 33
  4.5 Discussion 34
5. Assembly and Qualification 36
  5.1 Experimental Setup 36
  5.2 Experiment and Results 38
  5.3 Discussion 43
6. Conclusion 44
References 46
Appendix A 48
Appendix B 50
Appendix C 51
Appendix D 55
Appendix E 57
Appendix F 64

Acknowledgements

I am eternally thankful for the valuable advice and assistance my professor and supervisor provided me throughout this project. With their help, not only was this project possible to complete but a pleasure to work on. I would also like to thank Alan Grisel and Microsens for sponsoring and financing me.

I would like to thank CMi and the staff for answering all my questions, helping me solve issues during the fabrication and also quickly fix problems with machines so that I could complete my work. Each member of the staff was extremely helpful and supportive and it would have been impossible to complete the fabrication without them.

I would be nowhere without the support of my friends and family, particularly my parents and colleagues at LMIS1. Finally, I would like to thank my boyfriend for being there for me throughout the project and listening to me whenever I needed him.

1. Introduction

Gas chromatography systems using microcolumns (μcolumns), also called micro-capillaries, were first seen in the 1970s [1], becoming increasingly more common as fabrication processes matured. Today, this technology is used for detecting small amounts of potentially lethal and dangerous gases in homes, factories and airports [2] [3] [4]. Most applications desire or require small and/or portable devices, making micro-fabricated gas chromatography systems, also called μGC, particularly desirable. Systems that use microscale gas sensors and microcolumns are able to detect minute amounts of gases within small sample volumes in minutes, without the need for a large power supply or bulky packaging. Although not as sensitive as tabletop chromatographs, micro-fabricated gas chromatography systems are a viable portable option for on the field gas sensing [2] [5].

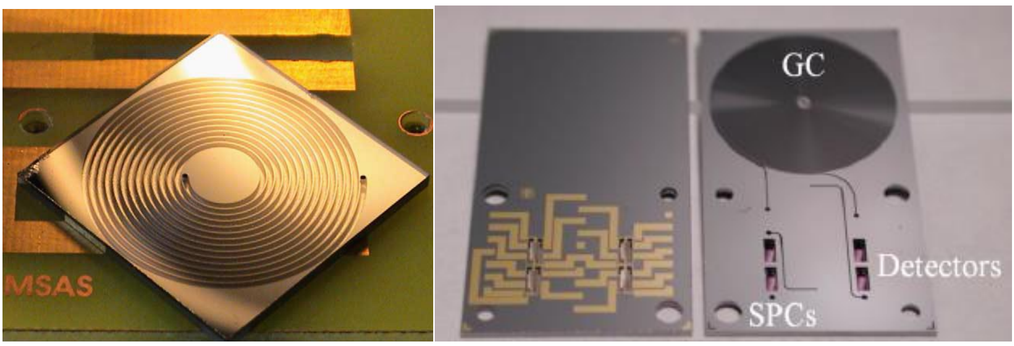

Figure 1 Two examples of microcolumns seen in literature (left, right references [5] [2] respectively)

Micro-fabricated gas chromatography systems can either be fabricated at once or assembled. For example, as seen in the left image of Figure 1, a fabricated microcolumn chip can be assembled to a variety of micro gas chromatography systems and replaced as needed. On the other hand, an integrated μGC, such as seen in the right image, provides the user with an integrated system that only requires fluidic and electronic connections.

Microcolumns are an important part of the gas chromatography process. Their task is to separate the different dilute species in a sample volume so that they individually reach the gas sensor at different times. By separating the species before they reach the sensor, a much simpler and cheaper gas sensor can be used that does not need to distinguish the type of gas, merely how much is present relative to the carrier gas transporting the dilute species. However, many factors control the quality of gas separation in the microcolumns, including the dimensions of the microcolumns, the surface treatment the microcolumns receive and the conditions in which the gases pass through the microcolumns.

Before this master thesis project, microcolumn chips, shown in Figure 2, had been fabricated by MicroSens with a serpentine geometry similar to those seen in literature [6] [7]. However, the results they received with their initial design proved unsatisfactory. Work completed

by a former master thesis student in collaboration with MicroSens [8] suggested that the transport of the gases from the microcolumn outlet to the gas sensor was a critical part of the chromatography setup and should be investigated further. In the gas chromatography system for this company, the microcolumn chip was assembled, in an open environment, directly above the gas sensor with a spacer to separate them and allow gas to escape after detection. It was unclear whether recirculation of the gases occurred after reaching the gas sensor or the gases dissipated into the open air before reaching the sensor. In general, the fluid dynamics of the gas chromatography assembly were unclear. This master thesis was completed in an effort to better understand the impact of the microcolumn geometry and gas chromatography assembly on the fluid dynamics and improve them as much as possible.

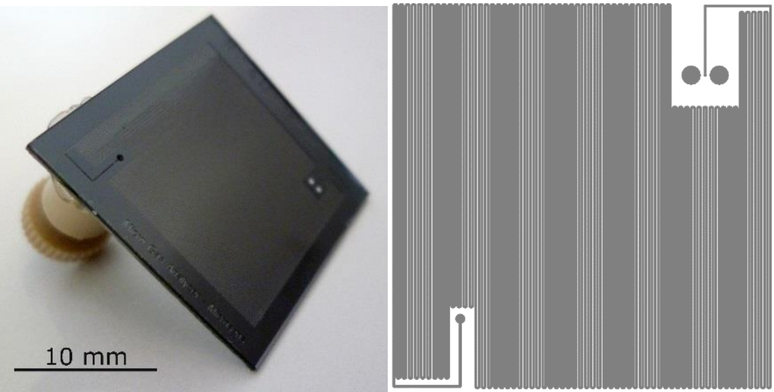

Figure 2 Left, microcolumn chip fabricated by MicroSens. Right, diagram of the original microcolumn geometry. Left image courtesy of Ulrike Lehmann.

The subject of this master thesis concerns the design, simulation, fabrication and qualification of new outlet geometries for microcolumns of a gas chromatography system developed by MicroSens, Switzerland. After a study of literature on the state of the art, several outlet geometries were designed and compared to the original outlet design with FEA (finite element analysis). The three most promising outlet geometries were chosen to be fabricated based on the velocity profiles calculated with the FEA. A second set of outlet geometries were simulated with FEA that included nozzles surrounding the outlets with even more promising results and two additional outlet designs were chosen to be fabricated. In total, five different outlet designs were fabricated with two different process flows in collaboration with CMi at EPFL.

For the qualifications, a new assembly was created for the experiments and a new hydraulic inlet connector was designed and fabricated with the mechanical workshop at EPFL. Four outlet geometries were tested without a stationary phase by injecting a sample volume with a dilute concentration of a volatile organic compound and analyzing the signal measured by a gas sensor placed at various positions with respect to the microcolumn outlet. The results for each section of the master thesis is discussed, as well as possible future experiments and adaptions that could be made to the microcolumn design and fabrication.

2. Theory

2.1 Gas Chromatography

Microcolumns are enclosed microchannels on the order of meters long with widths and heights on the order of microns. They are normally fabricated in crystalline silicon with traditional microfabrication technologies and sealed with glass through anodic bonding. A thin layer of polymer on the microcolumn surfaces or solid particulates packed into the microcolumns serve as the stationary phase and interacts with the dilute species to generate the gas separation [9] [10]. The stationary phase has different affinities for different gases and when sample volumes are pumped through the microcolumns, usually with air or helium as the carrier gas, these different affinities cause different gas species to separate from each other temporally. Depending on the gases that will be separated by the microcolumn, the stationary phase can be non-polar or polar, or multiple microcolumns can be connected in series with different stationary phases to separate gases in a complex sample volume, also called multidimensional gas chromatography [5] [11]. The microcolumns fabricated in this project will eventually use a PDMS coating as the stationary phase.

There are many types of gases sensors, including semiconducting metal oxide sensors, surface acoustic wave (SAW) sensors, magnetically-actuated resonators, and flame ionization detectors (FID) [2] [4] [12] [10]. In this master thesis, a tin-oxide resistive detector fabricated by MicroSens was used. To function as a sensor, the metal oxide layer is heated from 300-450°C, inducing the surface to create a O^- layer, if O_2 molecules are present above the surface, and creating a baseline conductivity. If other gas species are also present, electrons from the gas molecules are adsorbed by the metal oxide surface and change again the surface's conductivity [12]. The conductivity and therefore resistivity of the surface is proportional to the amount of molecules that are adsorbed.

The output from a gas sensor in a gas chromatography system will show peaks of each gas that is in the sample volume provided to the system, separated by time, as seen in Figure 3. Important parameters for gas chromatography are the peak height, arrival time of the gas to the sensor (beginning of the peak, also called retention time), the full width half maximum and the tail length.

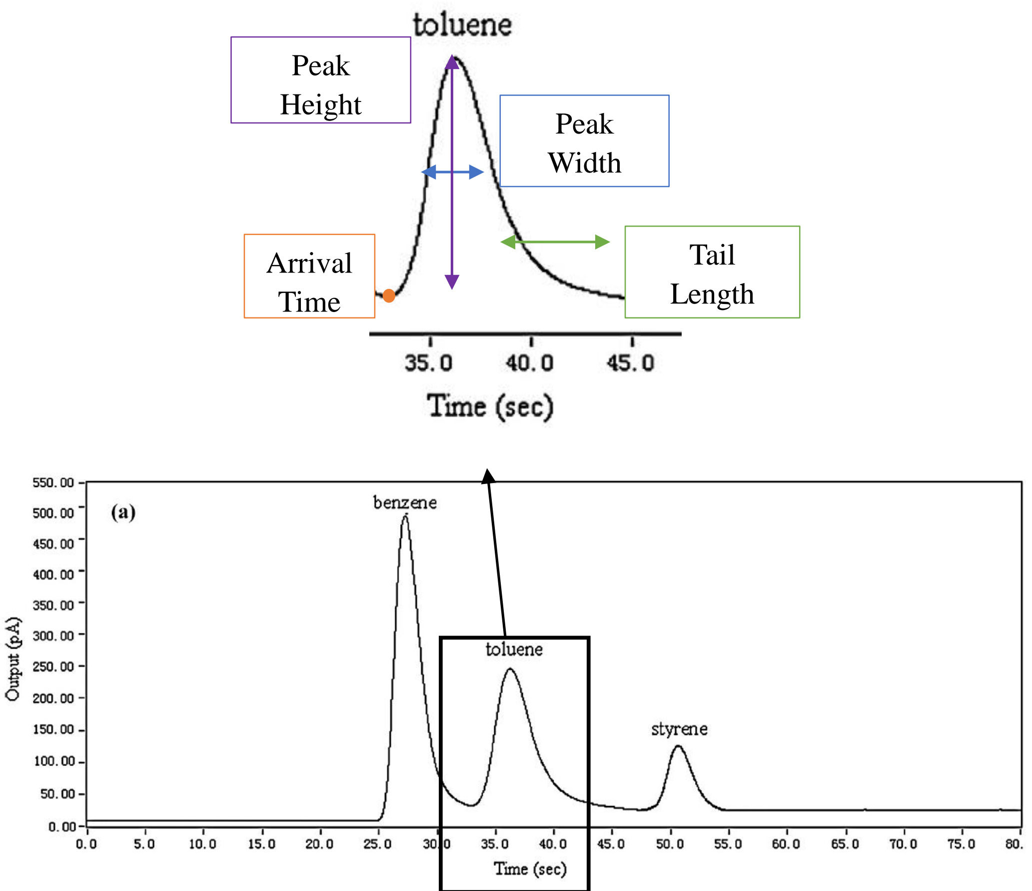

Figure 3 Top, close-up of bottom graph with descriptions of four parameters of interest in gas chromatography. Bottom, example of output from a gas chromatography setup with a sample volume including Benzene, Toluene and Styrene [7]

The quality of the microcolumn design and fabrication, as well as their utilization, influences the shape of the output signal from a gas sensor. Although in a perfect system the peak would be Gaussian, it is common to have asymmetry in the shape of the peak, such as peak tailing that broadens the peak's width. However, these can be corrected by improving the microcolumns in several ways, such as increasing the length of the columns, optimizing the velocity at which the sample volume moves through the microcolumns or correcting the microcolumn geometry. In this master thesis project, the geometry of the microcolumns' outlets was changed to improve the gas flow out of the microcolumn as well as optimize the assembly of the microcolumns to the gas sensor.

To compare different microcolumns, their efficiencies are gauged by calculating the number of theoretical plates, which is defined as:

$$N = 5.54\left(\frac{t_r}{w_{HM}}\right)^2 \quad (1)$$

Where t_r is the arrival time and w_{hm} is the full width at half maximum of the output signal generated by the sensor for a given gas sample. The idea of theoretical plates is originally from gauging the performance of distillation columns, where the theoretical plates are a series of zones within the columns where there would be equilibrium between gas and liquid phases [13]. Higher numbers of theoretical plates mean that the microcolumns are more efficient. The theoretical plate height is also used to compare different microcolumns and is defined as:

$$H = \frac{L}{N} \quad (2)$$

Where H is the theoretical plate height, L is the length of the microcolumn and N is the number of theoretical plates. Therefore, the shorter the height, the greater number of theoretical plates for a given length or shorter length for a given number of theoretical plates. Another way to express the theoretical plate height is through a modified Golay equation, which finds the band broadening of a sample volume that is transported through a rectangular cross-sectional microcolumn and interacting with the stationary phase [14]:

$$H = \frac{f_1 B}{u_0} + f_1 C_g u_0 + f_2 C_s u_0 + (f_2 u_0)^2 E \quad (3)$$

The first term is the static diffusion of the analyte in the carrier gas, the second the dynamic diffusion of the analyte in the carrier gas, the third the diffusion of the analyte in the stationary layer and the fourth the band broadening due to the instrumental dead times. The definitions for each of the variables and further information on Equation 3 can be found in [14].

The resolution between two peaks given by a gas chromatography setup, each of a different gas, is defined as:

$$R = 2\left(\frac{t_{R2} - t_{R1}}{w_{hm2} + w_{hm1}}\right) \quad (4)$$

Where t_{R1} and t_{R2} are the retention times of the first and second peaks and w_{h1} and w_{h2} are the widths at the bottom of the first and second peaks. As can be seen from the above theoretical

discussion, the width of the peak is an important parameter in regards to the separation strength of the microcolumn. The goal of this master thesis is to improve the peak width by changing the outlet geometry.

2.2 Fluid Dynamics

In microscale fluid dynamics, the fluid flow is laminar due to a small hydraulic diameter and fluid velocity. However, unlike in liquid microfluidics, gas microfluidics must work with compressibility and low viscosity and possibly slip flow. The Reynolds number Re can be calculated to find the ratio of inertial forces to viscous forces, defined as $\frac{\mathbf{v}D_H}{\nu}$ (v is the average flow velocity, D_H is the hydraulic diameter and ν is the kinematic viscosity). For the microcolumns produced in this master thesis, the Reynolds number is about 50, meaning that laminar flow is present and inertia plays the less dominant role in fluid dynamics, though is not completely negligible as in Stokes flow [14].

The velocity profile of the fluid as it moves through the microcolumn will be parabolic in shape perpendicular to the direction of the flow and flat parallel to the direction of the flow. A calculation of the Knudsen number Kn, defined as λ/d (λ is the mean free path and d is the characteristic length scale of the system) for our system gives of value of $.5*10^{-4}$, meaning that our system is in the continuum flow regime and a no-slip condition is valid for the boundaries of the velocity profile [14].

The microcolumns take advantage of the Dean effect at curved portions to focus the different gas species' volumes being created as the sample volume moves through the microcolumn [15]. Some microcolumn designs consist entirely of curved columns in a spiral design to take the most advantage of this effect, while other designs simply curve the ends of microcolumns that are in a serpentine shape [6]. A previous master thesis project in collaboration with MicroSens [8] showed that there was no significant difference between the two geometry designs in terms of efficiency, arrival time or peak widths with the parameters used in their experiments. In this thesis project, a serpentine geometry was used.

3. Finite Element Analysis

To better understand the effect the outlet geometry of the microcolumn has on the air flow onto the gas sensor, FEA (finite element analysis) was used to simulate many different outlet geometries. Initially, the company's original microcolumn to gas sensor assembly was designed and simulated as a 3D model in COMSOL Multiphysics® with the Fluid-Structural Interaction Module. Figure 4 and Figure 5 show the volume created for the simulation, including a chip and sensor, open air volume, outlet cylinder and microcolumn connected to the outlet. For the rest of this report, the original outlet geometry will mean the outlet geometry fabricated by MicroSens before this master project. The chip and sensor within the model are simply solid structures resembling the pieces in real life and are rigidly fixed as to not move during the simulation.

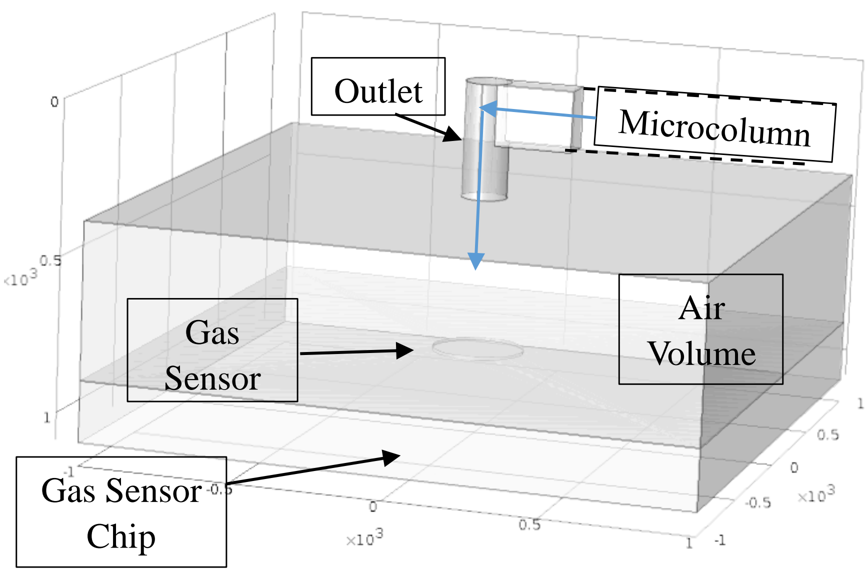

Figure 4 MicroSens original outlet to sensor assembly designed as a 3D model in COMSOL Multiphysics®. Blue arrows indicate the air flow from the beginning of the microcolumn geometry into the outlet and then into the air volume on top of the gas sensor.

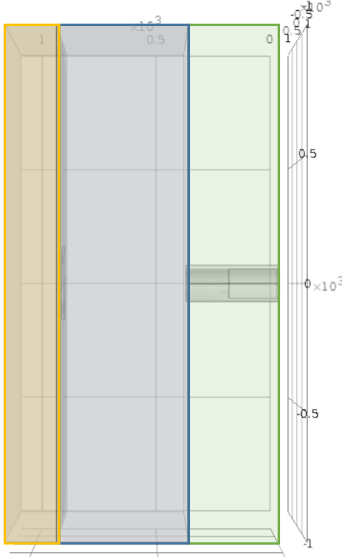

Figure 5 Original outlet geometry. Green rectangle designates the silicon that the microcolumn and outlet are fabricated in in real life, which was not included in the 3D model. The blue rectangle indicates the air volume and the yellow rectangle for the chip and gas sensor.

The outlet cylinder was 380 μm tall and 150 μm wide, as has been fabricated by the company, and the microcolumn was 120 μm wide by 200 μm tall by 300 μm long to simulate the end of a 2.1 m microcolumn into the outlet. The air volume was 2 mm by 2 mm by .5 mm, to simulate the open air currently present in the gas chromatography setup. The chip was a solid silicon block of dimensions 2 by 2 by .2 mm^3 with a 10 μm tall cylinder of 300 μm width on top to act as the gas sensor. The inlet for the simulation was at the entrance of the microcolumn and air was used as the fluid. The outlets were the sides of the air volume not in contact with the outlet or the chip. The meshing was physics-generated and was set to normal for most simulations, except when the number of elements caused the analysis to take extraordinarily long.

The following boundary conditions were used in the FEA:

- Fixed constraint on all silicon geometries
- Laminar inflow of .674 m/s with an entrance length of 2.1 m
- Non-viscous pressure outflow
- Slip wall conditions, close to the behavior of air within a microchannel

Of interest to understand from all the simulations was how the velocity of the air changed as it moved from the outlet onto the gas sensor. A successful microcolumn chip should be designed so that the sample flows from the outlet quickly onto the sensor and then quickly away from the sensor so that it can refresh. A velocity field arrow diagram was created from the simulation results, as shown in Figure 5 for the original outlet geometry. Figures 6 and 7 show the velocity magnitude and z velocity field (z axis is perpendicular to the surface of the sensor) calculated on an x-y slice

10 μm above the gas sensor. Several other distances above the gas sensor were also measured (not shown in this report) to better understand how the magnitude and direction of the air flow changed as it moved from the outlet through the air volume to the gas sensor and chip surface. As can be seen in Figure 6, Figure 7 and Figure 8, there was a dramatic decrease in the magnitude of the velocity once the air exits the outlet into the air volume until it was nearly negligible at the gas sensor surface. There was no recirculation of the air, only dissipation of the velocity before reaching the gas sensor.

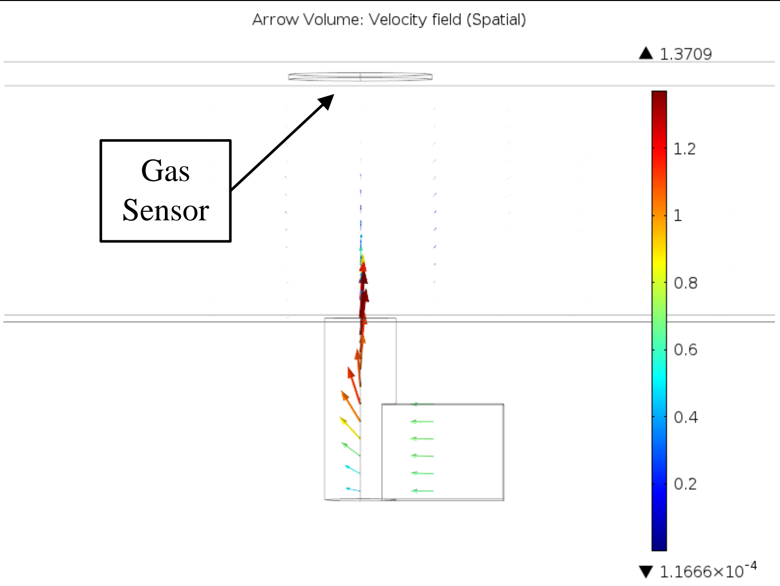

Figure 6 Velocity field visualized by arrows with length and color determined by the velocity magnitude at each arrow. Original outlet geometry.

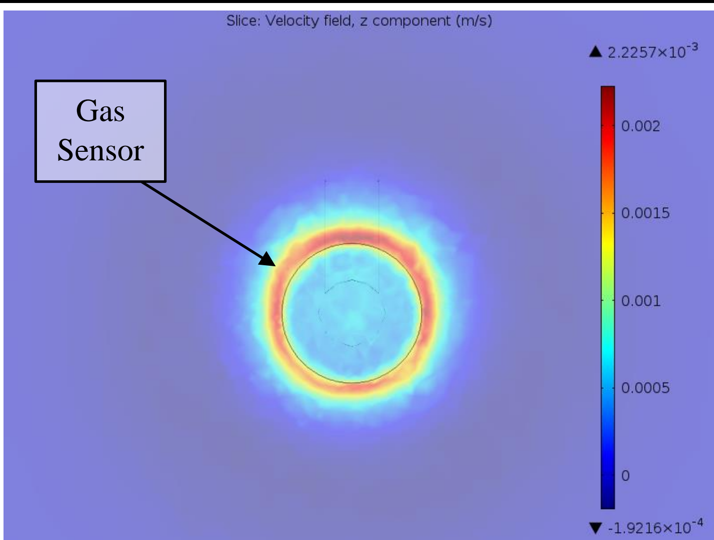

Figure 7 Z velocity field calculated on a x-y slice 10 μm above the sensor surface in the simulation. Original outlet geometry.

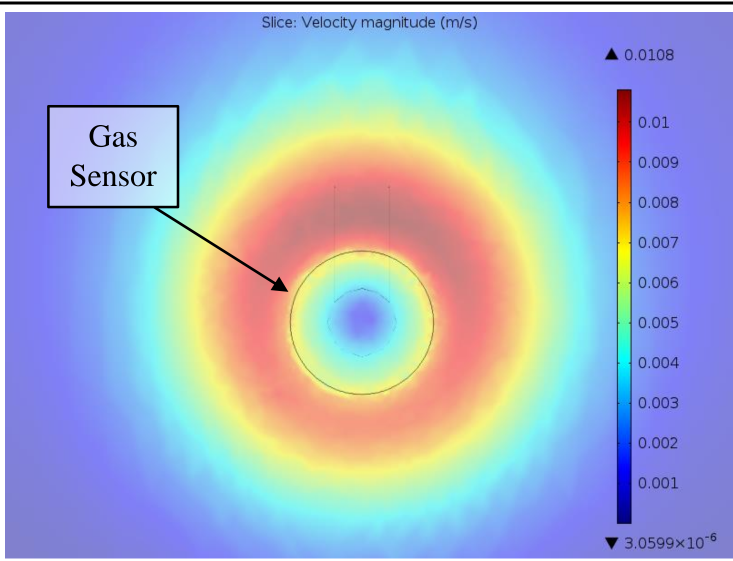

Figure 8 Velocity magnitude calculated on a x-y slice 10 µm above the sensor surface in the simulation. Original outlet geometry.

The sensor and chip assembly as well as the air volume in between the gas sensor and the microcolumn outlet inside the gas chromatography setup have larger dimensions in real life than designed in the FEA, but were downsized in the FEA to decrease computation time. To ensure that the decreased size did not strongly affect the simulation, three different air and chip volumes (1.5 by 1.5 mm^2, 2 by 2 mm^2 and 3 by 3 mm^2 chip surface area, air volume and chip depths kept at .5 mm and 2 mm respectively) were tested with only a .02 m/s change from the smallest to largest volume. The results can been seen in Appendix A for an original outlet geometry with an outlet width of 120 µm.

Three sets of simulations were completed in this master thesis project in an effort to see possible ways the outlet geometry could affect the velocity profile. In addition to simulation runs, several other simulation models and calculations were made, see Appendix A, B and C and the 2D simulation model described later on. Depending on the outlet conditions, both the air and chip volumes were slightly smaller or larger. The different outlet geometry models were kept as similar as possible in terms of boundary conditions and geometry to the original outlet geometry model for a valid comparison of the velocity profiles.

3.1 1st Simulation Run

This simulation run focused on manipulating the width of the outlet cylinder in the original outlet geometry to see its effect on the velocity profile. The following outlet cylinder widths were tested: 120 µm, 150 µm, 200 µm, 250 µm, 300 µm, 400 µm. The minimum width was determined from the width of the microcolumns used by the company, which was 120 µm. Any smaller outlet widths would create an unsmooth transition from the microcolumn to the outlet by introducing

corners where recirculation could occur. These 3D models were created with a simpler geometry than shown in Figure 4 in order to significantly decrease computation time without much change to the fluid dynamics. It was found that increasing the outlet cylinder width further decreased the gas velocity before exiting the outlet and that it would be better to have smaller widths because it concentrated the air flow. The velocity arrow field results for an outlet width of 120 µm can be seen in Appendix B. The below table shows the average velocity magnitude, maximum velocity magnitude and average velocity magnitude for the z component on the sensor surface for each outlet width.

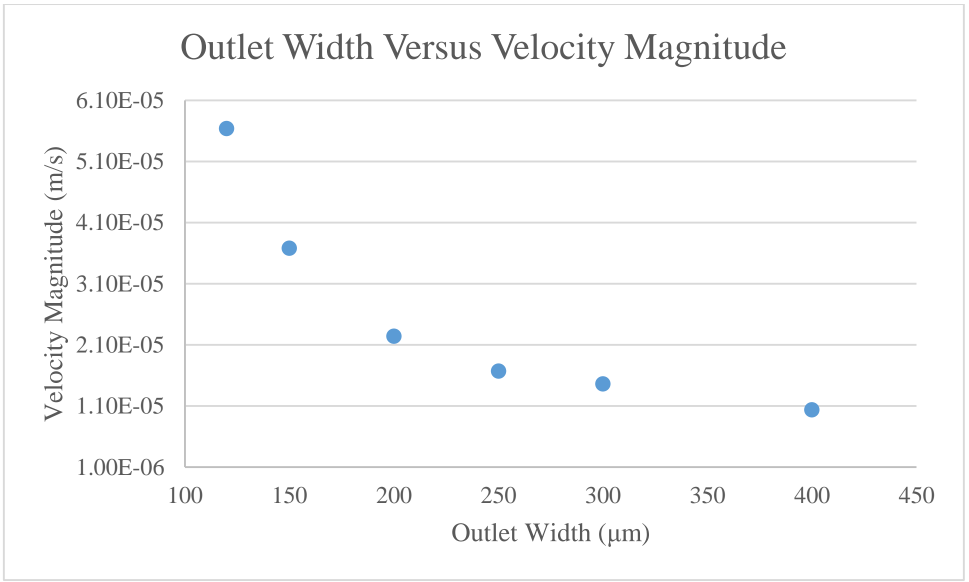

Figure 9 Influence of outlet width on average velocity magnitude measured on the sensor surface within the FEA.

3.2 2nd Simulation Run

Several side outlet geometries were designed and simulated to see the change in the velocity profile over the gas sensor. Some geometries contained a 100 µm thick glass volume above the outlet, simulating a glass cover that could be created during fabrication. Two geometries contained slits beneath the outlet to simulate an open space directly underneath the outlet that would be surrounded by 380 µm thick silicon, to channel the air flow more directly at the gas sensor. The below table provides the names and descriptions of the outlet geometries tested. Figures of all the geometries can be found in Appendix C.

Name of Outlet Geometry	Description of Outlet Geometry
Smaller original outlet	Original outlet geometry but with a 120 µm wide outlet cylinder to focus the air flow before entering the air volume.
Corner original outlet	Original outlet geometry but designed that it would be in the very corner of the microcolumn chip for easier assembly to the gas sensor. Also with a 120 µm wide outlet cylinder. A 10 um thick silicon piece was included to simulate the corner of the microcolumn chip.
Side outlet	Instead of an outlet that is perpendicular to the microcolumn, the microcolumn would continue to the end of the chip, opening an outlet on the chip's side.
Side outlet with cover	A side outlet geometry with a cover on top of the outlet to keep the air flow from moving up directly after exiting the outlet. The cover is 100 µm thick and 300 µm long.
Side outlet with cover and slit	A side outlet geometry with a cover as well as a slit underneath the microcolumn that opens up the outlet below before the edge of the chip, allowing air to move downward and forward out of the outlet onto the gas sensor. The slit is 300 µm long and would cut through 180 µm of silicon if fabricated.
Corner side outlet	A side outlet geometry but designed as if the outlet was in the corner of the microcolumn chip, so that the cover is triangular in shape. The cover is again 100 µm thick and 300 µm long.
Corner side outlet with slit	A corner side outlet geometry but with slits as seen in the side outlet with cover and slit.

As can be seen in the above list, two general types of outlet geometries were tested: those with outlets perpendicular to the surface of the gas sensor and those with outlets parallel to the surface of the gas sensor. One reason for designing and simulating the side outlet geometries was to adapt the microcolumn design for gas chromatography with resonating sensors. Initially, there was fear that the perpendicular outlet geometries would introduce too strong an air flow on top of a resonating gas sensor, which would affect its ability to sense. However, analytical calculations of the deflections of membranes with pressures calculated from the FEA of several outlet geometries found that the maximum deflections are negligible and therefore perpendicular outlet geometries as well as side outlet geometries can be used in gas chromatography with resonating sensors. More details of the analytical calculations can be found in Appendix D.

Another reason for designing side, as well as corner, outlets was to find geometries that could be assembled closer to the gas sensor. At the moment, a spacer and wire bonds allow a minimum height difference of 500 µm between the outlet and sensor. The hope is that outlets designed in this project can be assembled during packaging closer to the sensor without interfering with the wire bonds. Initially, all outlet geometries were tested at a distance of 500 µm above the sensor.

The average velocity magnitude on the surface of the sensor inside the models was used as the benchmark for determining good or poor geometries. The results from the FEA for each outlet geometry model was also qualitatively visualized by the velocity field in arrows from the outlet to the sensor, as well as making slices 1 µm and 10 µm above the sensor that gave the velocity magnitude and velocity field perpendicular to the sensor surface, such as seen earlier in this section. Figure 10 shows the calculated velocity magnitude for the seven geometries described above, normalized to the original outlet's velocity magnitude.

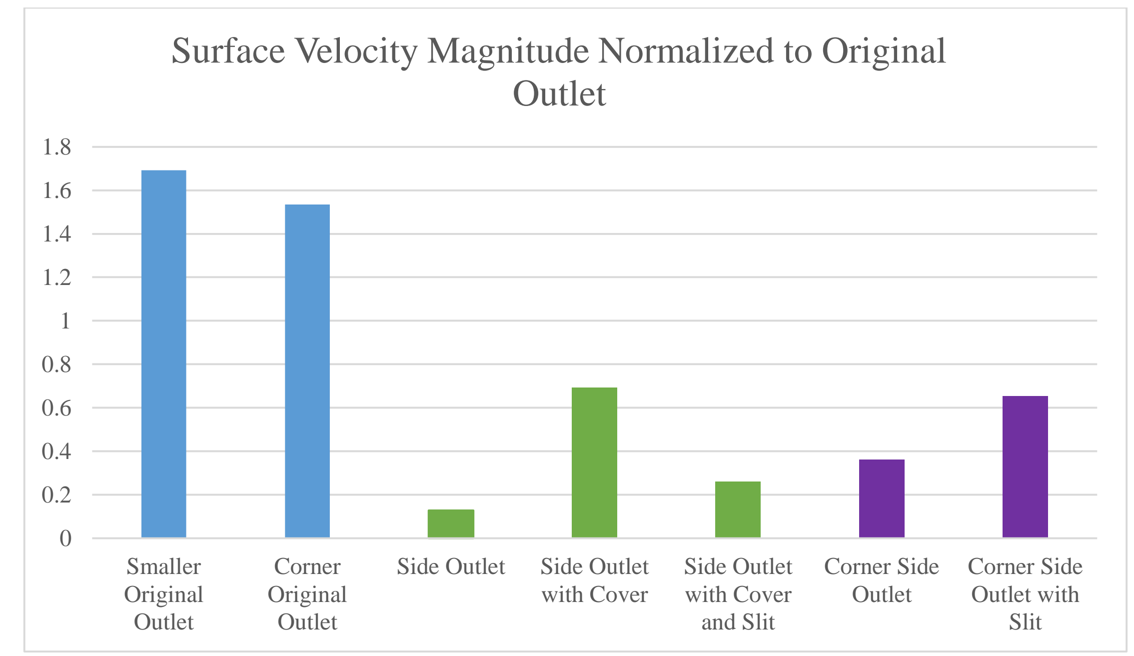

Figure 10 Surface velocity magnitude results for the outlet geometries described in the table on the previous page. Blue bars denote the modified original outlets, green and purple for side outlets.

The modified original outlet geometries show an improvement on the velocity magnitude, while the side outlet geometries do not show a large improvement. The velocity arrow field results for three geometries are shown below. The arrows' colors are equal to the velocity magnitude measured at that point and the arrows' sizes are scaled on the velocity magnitude, but were scaled differently for some of the models to better see the arrows in the diagrams.

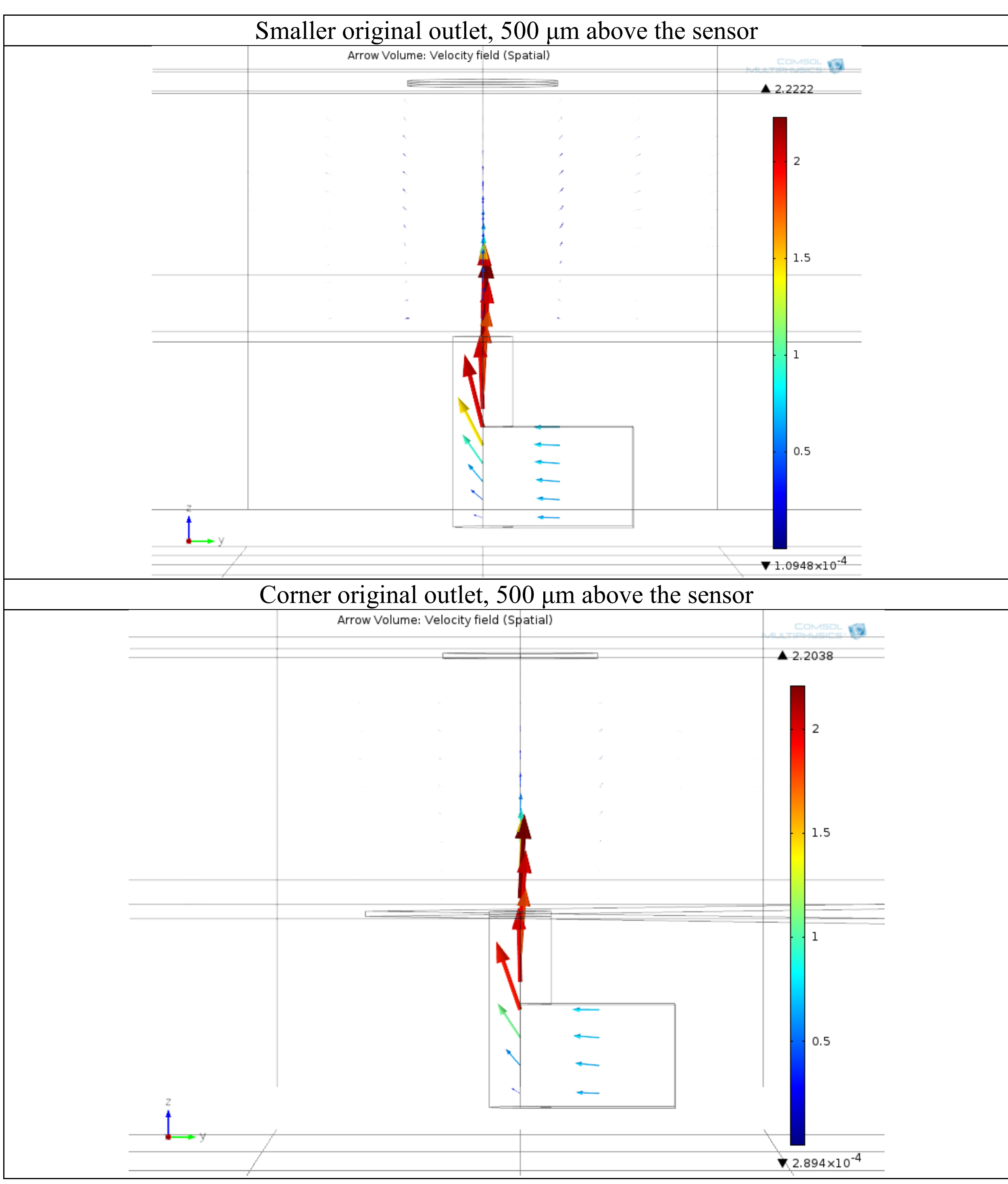
Smaller original outlet, 500 µm above the sensor
Arrow Volume: Velocity field (Spatial)
▲ 2.2222
2
1.5
1
0.5
▼ 1.0948×10^-4
z
y
Corner original outlet, 500 µm above the sensor
Arrow Volume: Velocity field (Spatial)
▲ 2.2038
2
1.5
1
0.5
▼ 2.894×10^-4
z
y

Corner side outlet with slit, 500 μm to the left and 300 μm above the sensor

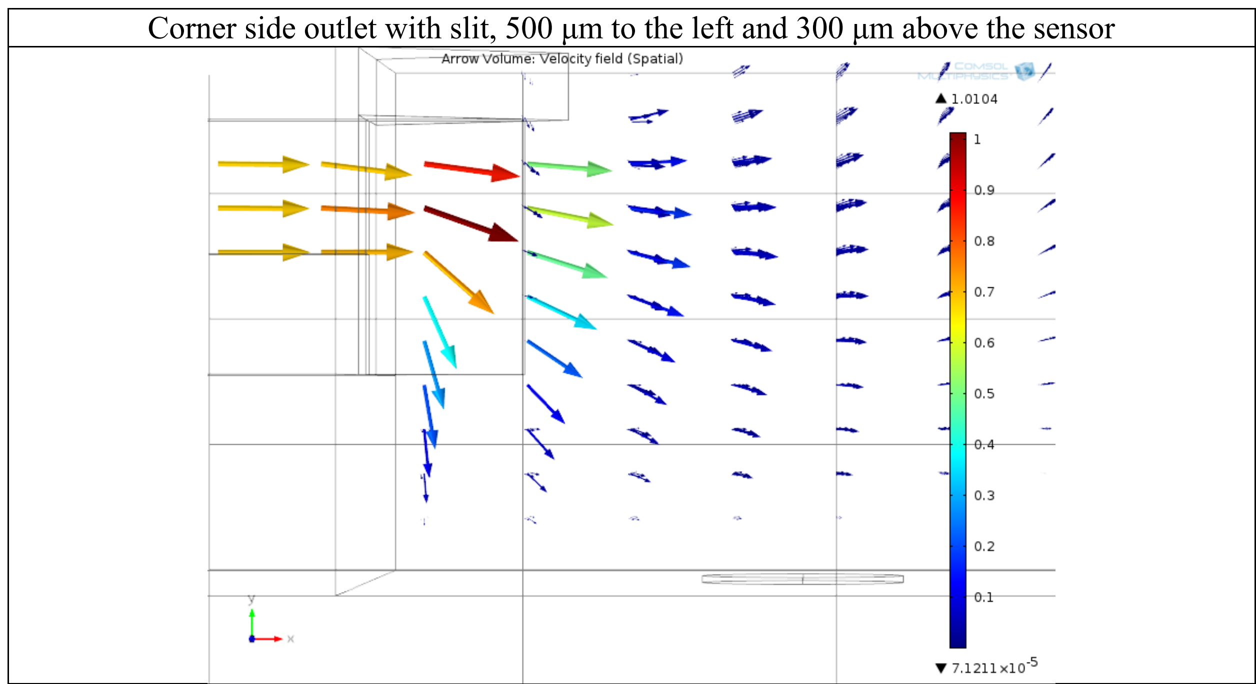

In all the calculated results for the outlet geometries, the velocity dramatically decreases after the outlet, though placing geometries to better control the flow of the fluid did increase the velocity magnitude calculated on the surface of the sensor. In the side outlet geometries, the fluid mostly flowed parallel to the sensor surface. Moving all the outlets closer to the sensor increases the velocity magnitude. For example, moving the corner side outlet geometry with slits to 150 μm above and 150 μm to the left of the gas sensor improves the velocity magnitudes seen near the sensor. For the side outlets, adding a cover or slits helped to direct the air flow more directly onto the gas sensor and with higher velocity magnitudes.

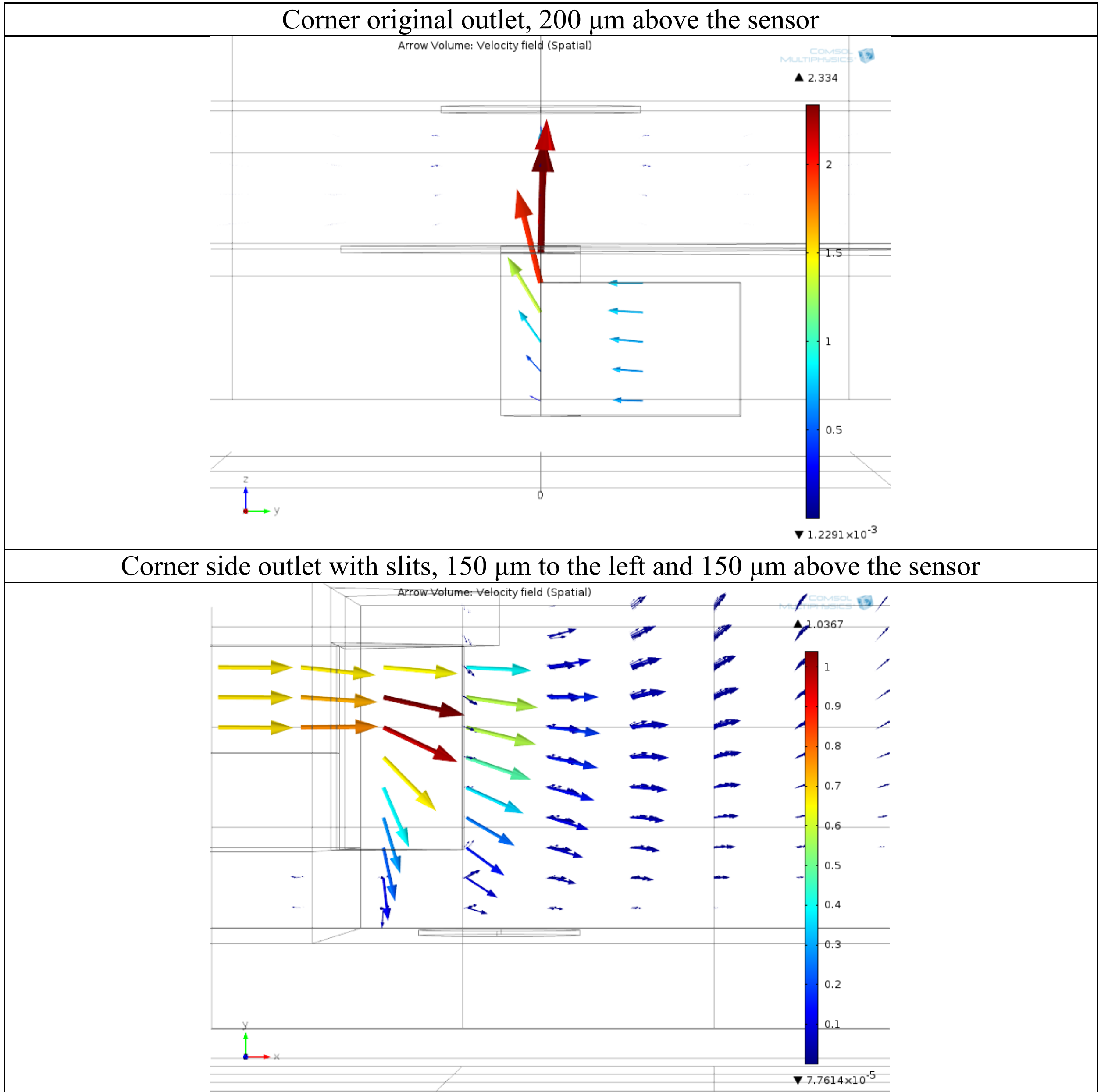

3.3 3rd Simulation Run

In the final set of simulations, a nozzle was designed on top of the corner original outlet geometry to see if it was possible to focus the flow like the cover and slit did for the side outlet geometries. Based on earlier results of decreasing the outlet cylinder width to focus the air flow, four inner widths were tested for the nozzle cylinder: 60 µm, 80 µm, 100 µm and 120 µm. The geometry for a 120 µm inner diameter nozzle at the end of the outlet can be seen in Figure 11.

Figure 11 Corner original outlet geometry with a nozzle added at the outlet exit into the air volume.

The table below shows the velocity arrow field results for the four inner widths. As the inner width is increased, the focusing power decreases. Compared to the corner original outlet geometry, there was an increase in the velocity profile and the air flow is better directed onto the gas sensor.

60 µm Nozzle Inner Width
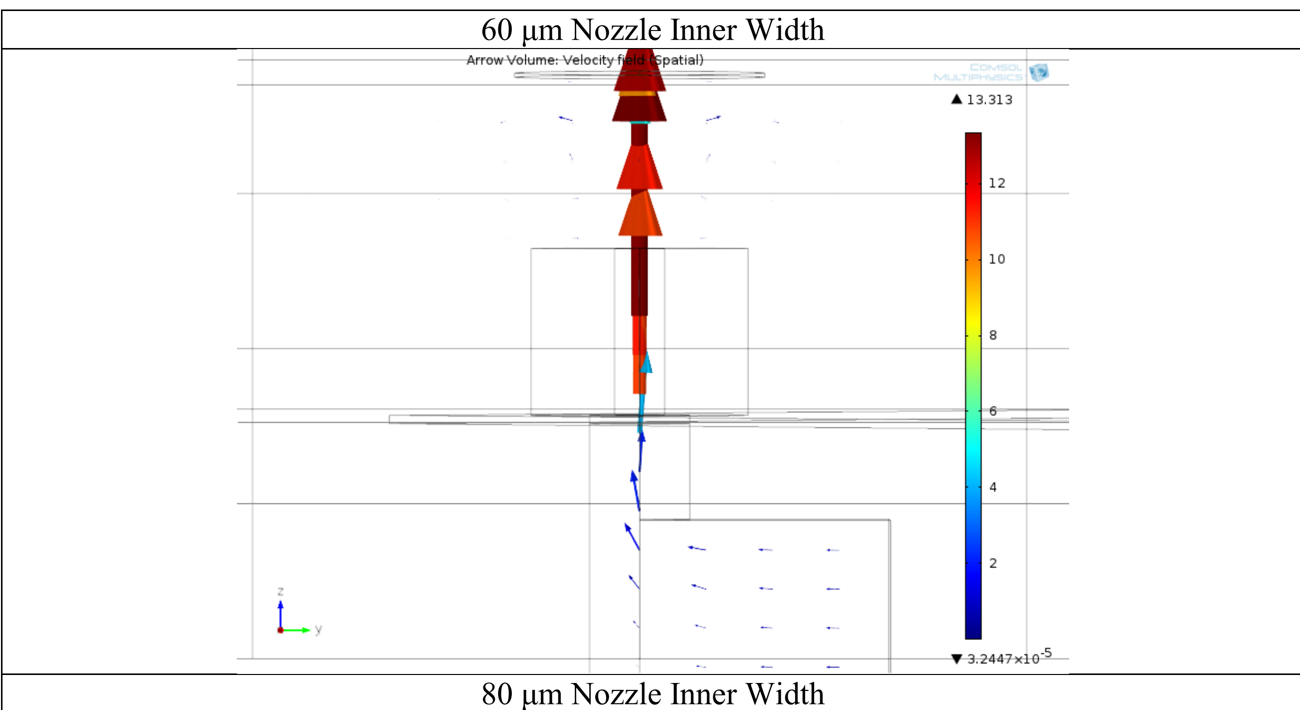
80 µm Nozzle Inner Width

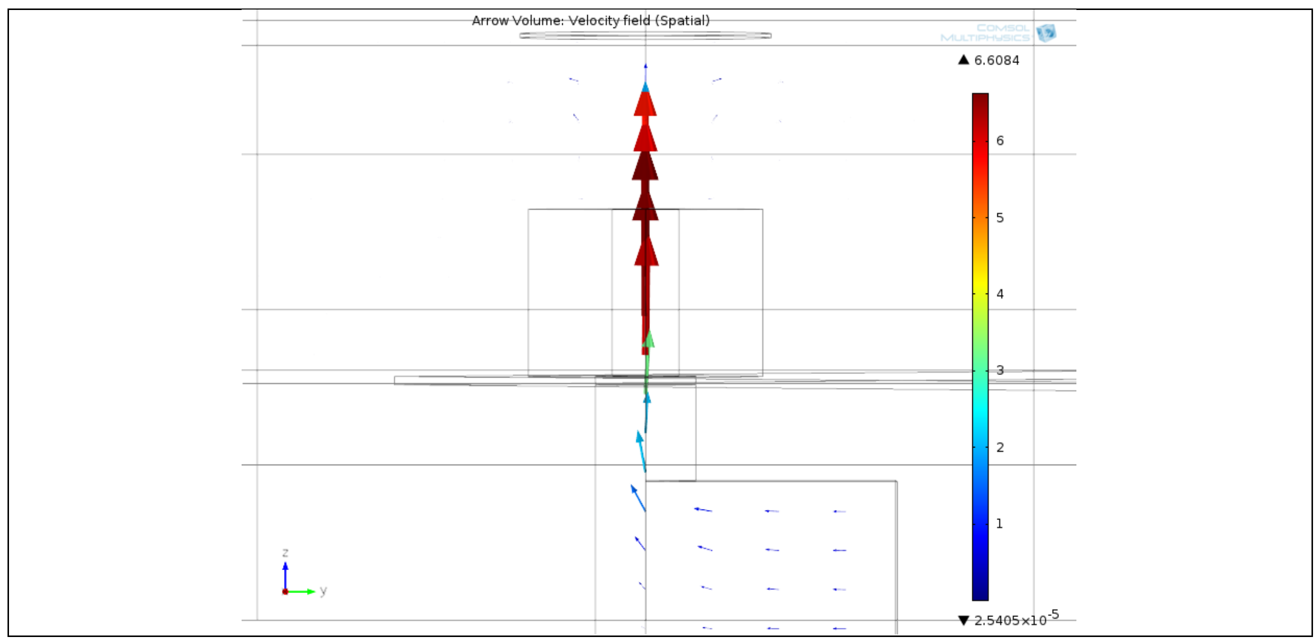

100 µm Nozzle Inner Width

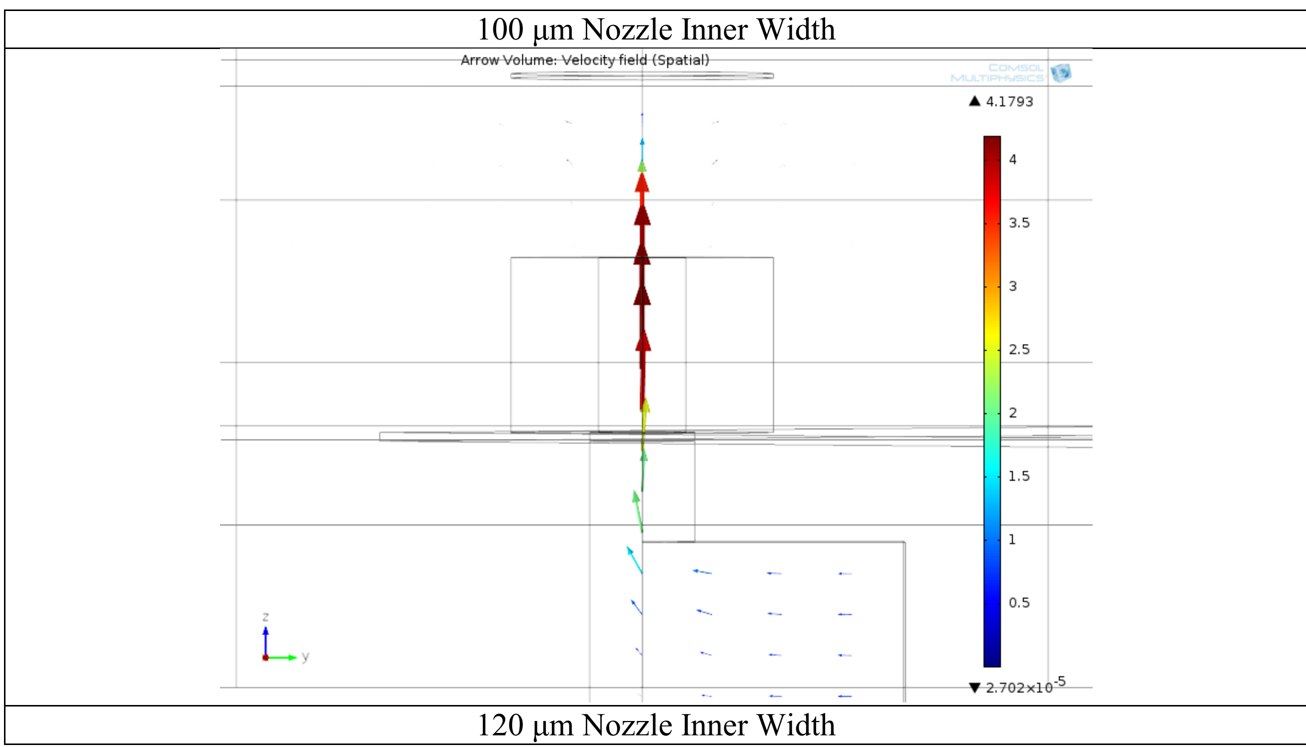

120 µm Nozzle Inner Width

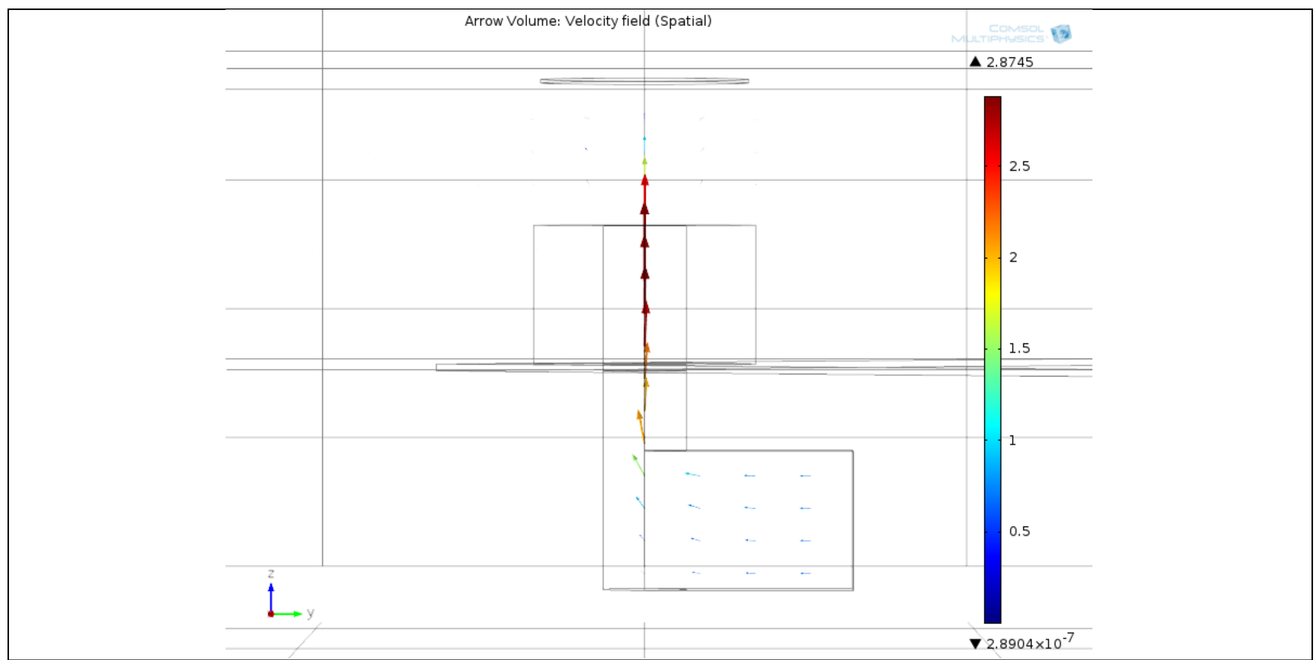

When the velocity magnitudes calculated on the surface of the sensor are compared between a nozzle or nozzle-less geometry, shown in Figure 12, for two different heights, one can see that the nozzle greatly improves the velocity magnitude measured on the surface of the sensor.

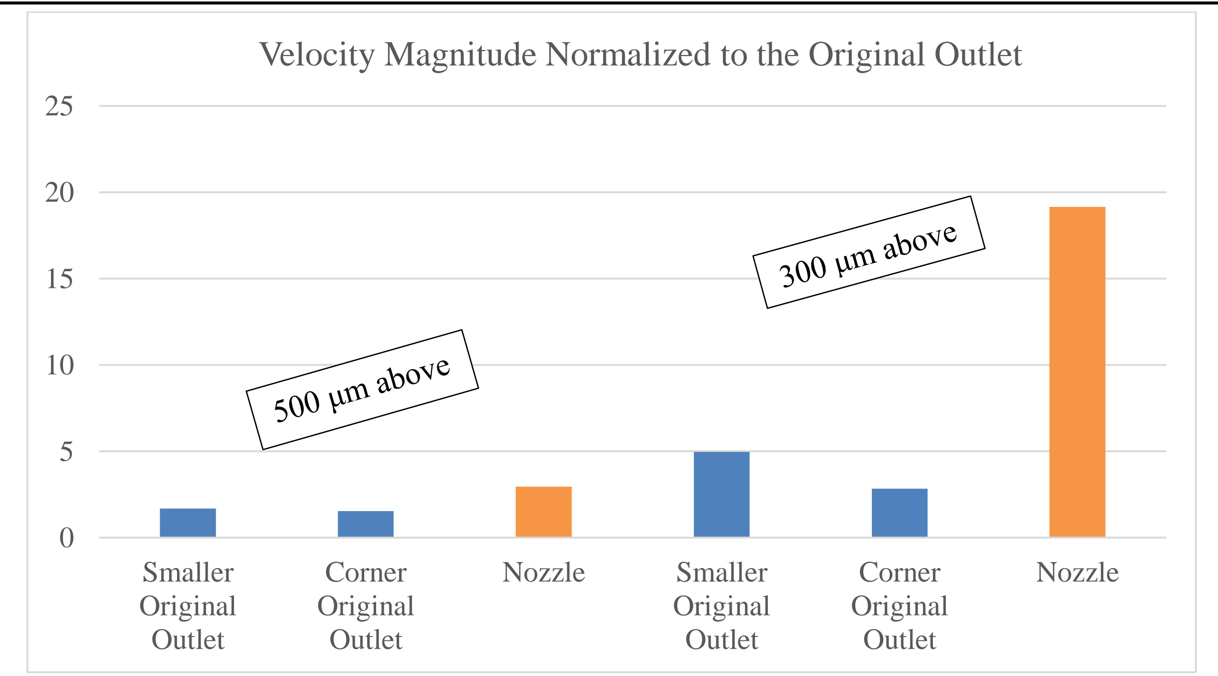

Figure 12 Modified original outlet geometries compared to a nozzle geometry at heights of 500 µm and 300 µm above the sensor.

3.4 Discussion

The numerous FEA models created during this part of the master project provided clarifying information on the fluid dynamics of the gas chromatography assembly being used by Microsens. It is clear that the air flow exiting the outlets has a low velocity and loses much of its speed before reaching the sensor, unless the outlet is very close to the sensor. No recirculation occurs of old sample volumes into new samples after interacting with the gas sensor. It is therefore important to have outlet geometries that would allow for close assembly to the sensor, such as the corner outlet geometries. The side outlet geometries generally have smaller velocity profiles than the original outlet geometries, but may later prove to provide better signal peaks due to the air flow's aid in refreshing the gas sensor after the sample volume has been detected. Both side outlet and original outlet geometries could be used with resonating sensors since both types have too small of velocity magnitudes to have any impact on the resonance. Finally, nozzles greatly improve the air flow and velocity profile in comparison to the modified original outlet geometries.

Three outlet geometries from the second simulation run were chosen to be fabricated: smaller original outlet, corner original outlet and corner side outlet with slits. The corner outlets can be potentially assembled closer to a gas sensor than the original outlet and the smaller original outlet will be used as the baseline geometry for later comparisons in experiments. The nozzles were also chosen to be fabricated on the smaller original outlet and the corner original outlet. For the nozzle width, although the simulation results showed that decreasing the inner width increased the focusing of the air flow onto the gas sensor, concerns about the difficulty of fabricating the smaller inner widths led to choosing the 120 μm inner width for the nozzle.

4. Fabrication

Two process flows were used during the fabrication. In both process flows, double-side polished silicon wafers were processed on both sides, the topside for the microcolumns and the backside for etching through the inlets and outlets. In the first process flow, no thermally grown silicon oxide was used on the silicon wafers and positive photoresist was the masking material, while in the second process flow, 1.5 µm of silicon oxide was used on both sides of the silicon wafers as a masking material. The microcolumns were closed by anodic bonding and the individual microcolumn chips were diced outside of the cleanroom. The first process flow can be seen in Table 1 below while Table 2 shows the second process flow. The runcards for both process are in Appendix E.

Step 1 Photolithography	Step 4 Photolithography
40um Silicon	
Step 2 DRIE	Step 5 DRIE Backside
Step 3 Anodic Bonding	
Borofloat	

Table 1 1st Process Flow

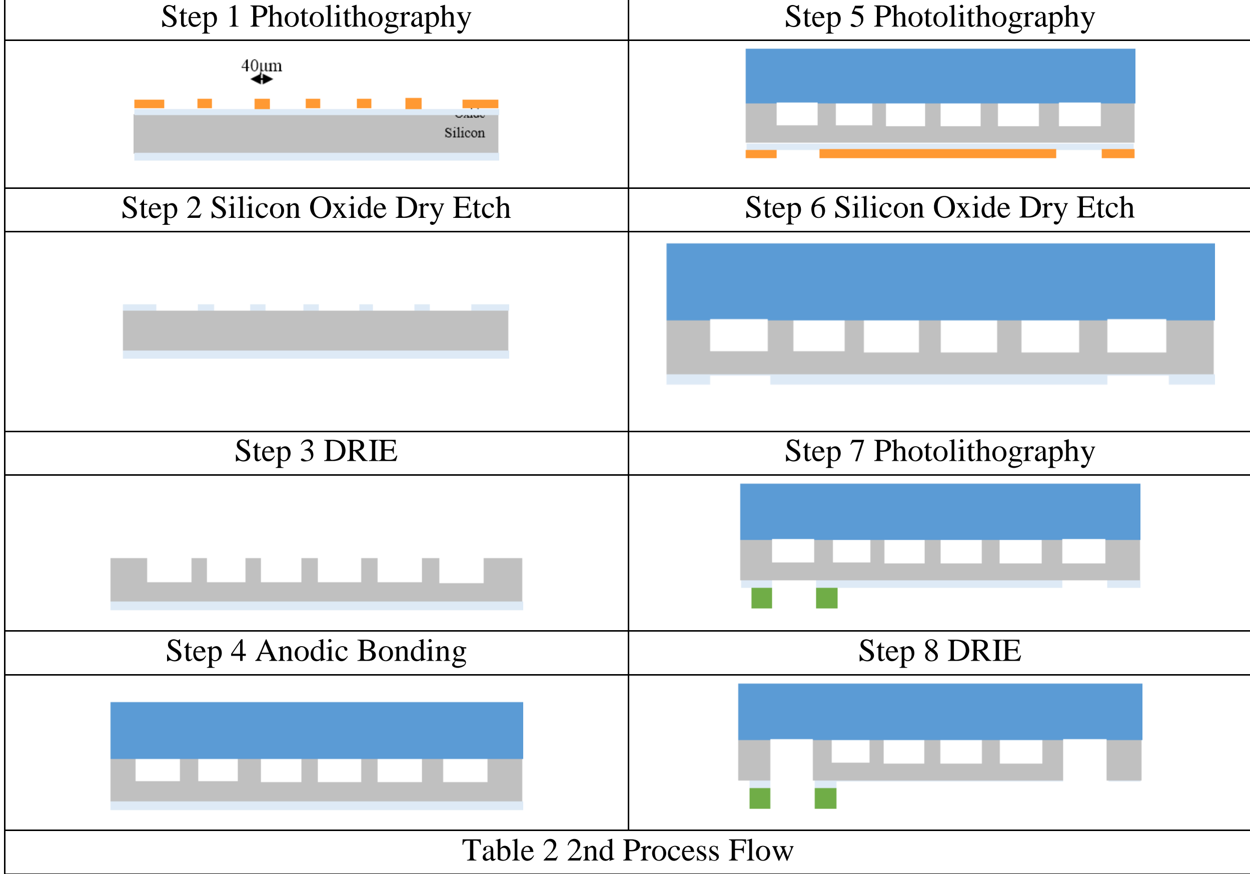

Table 2 2nd Process Flow

In the end, five different outlet designs were fabricated:

- Smaller original outlet
- Corner original outlet
- Original outlet with SU8 nozzle
- Corner original outlet with SU8 nozzle
- Corner side outlet with slits

The above designs were fabricated in order to validate the simulations described in the above section, as well as to have the opportunity to experimentally test the same outlet designs with and without nozzles.

4.1 Mask Design

The mask designs for the two process flows were designed with Clewin 4 and are shown in Figure 13. When a mask aligner was used to expose the pattern onto photoresist, the nine chip mask design was used, shown on the left side of Figure 8. When a direct laser writer was used for the exposure, the seven chip mask design was used, shown on the right side of Figure 8, so that the bottom chips would not be patterned too close to the wafer edge. In both designs, dicing

marks were placed in between the microcolumn chips as well as symmetric alignment marks that were all provided by the CMi staff. Each mask layer contained a number designating the order that it would be used as well as the date that the mask designed was finalized.

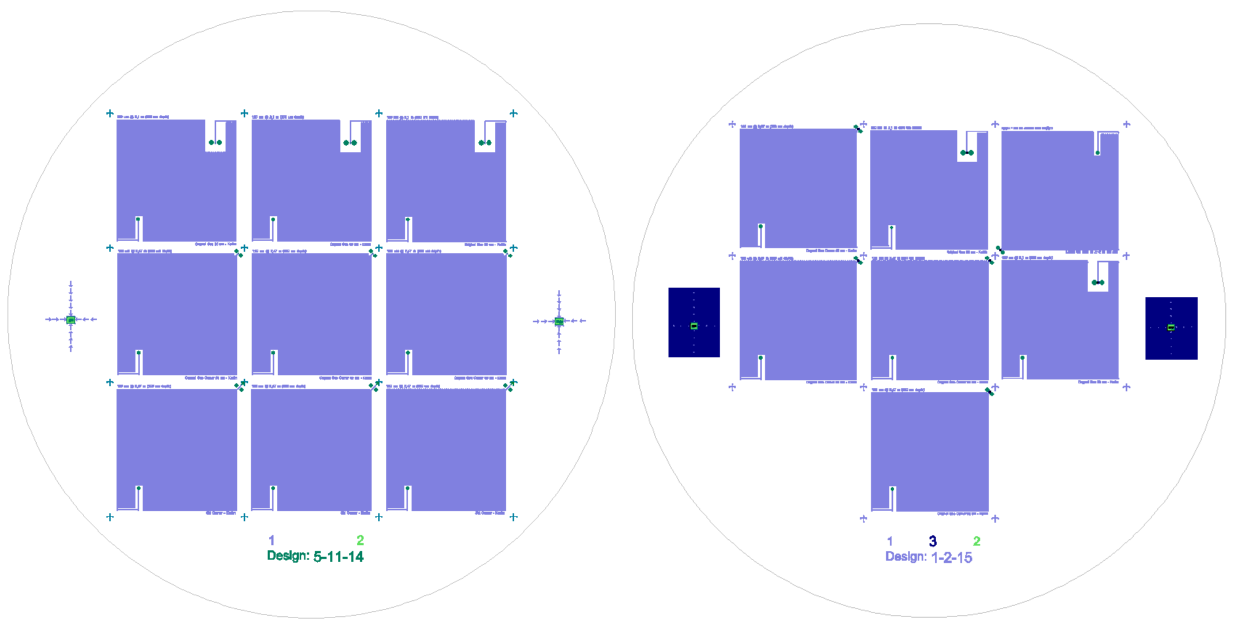

Figure 13 Two mask designs used during fabrication of microcolumn chips.

Two masks were necessary for the first process flow, one topside mask for etching the microcolumns and a second backside mask to etch the inlets and outlets. Three different outlet geometries were used: Smaller original outlet, corner original outlet and corner side outlet with slits. Other than slightly adapting the microcolumn design so that the outlets were at the corner of the chip instead of closer to the middle of the chip, no other changes were made to the company's original design (the original microcolumn design can be seen in Figure 2). The original microcolumn was 2.1 m long but when the microcolumn geometry was adapted for the new columns, the length increased to 2.5 m. The purple geometries were the topside mask while the green geometries were for the backside mask. The masks overlap at the inlets and outlets, where the silicon wafer will be etched through entirely. For the corner slit outlet geometry, at the end the fabrication, the triangular piece at the end of the outlet becomes glass. The three outlet geometries in the mask design can be seen in Figure 14.

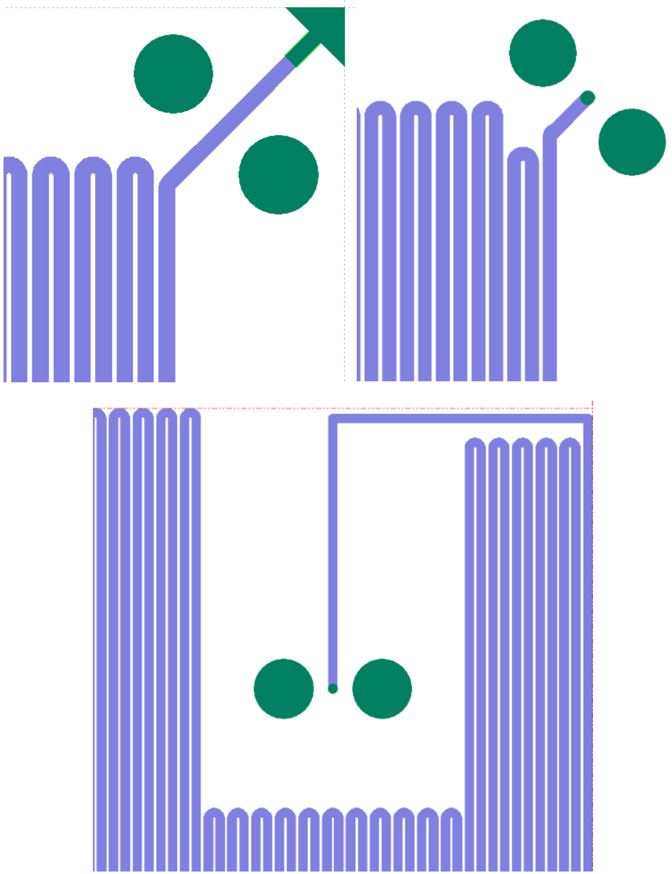

Figure 14 The three outlet designs used in the first process flow. Top left, corner side outlet with slits. Top right, corner original outlet. Bottom, smaller original outlet. The large green circles are for alignment during assembly.

For the second process flow, two or three masks were necessary, depending on if nozzles were fabricated on the wafers. If SU8 nozzles were fabricated, three masks were necessary: the first to etch the microcolumns, the second for etching the oxide mask to make the inlet and outlets on the wafer backside and the third to create the SU8 nozzles. Based on advice from the CMi staff, the nozzles were fabricated partially on bare silicon and partially on the silicon oxide mask for better overall adhesion to the wafer surface. If no SU8 nozzles were fabricated, then only two mask designs were necessary: the first for etching the microcolumns and the second for etching the oxide mask to later etch the inlets and outlets. Two outlet geometries were used, shown in Figure 15: corner original outlet and smaller original outlet. The dark blue geometries were the cylinders that became SU8 nozzles around the outlets on the backside of the microcolumn chips. If SU8 nozzles were not placed around the outlets, then the green outlet geometries were changed back to the same dimensions as in the first process flow mask design.

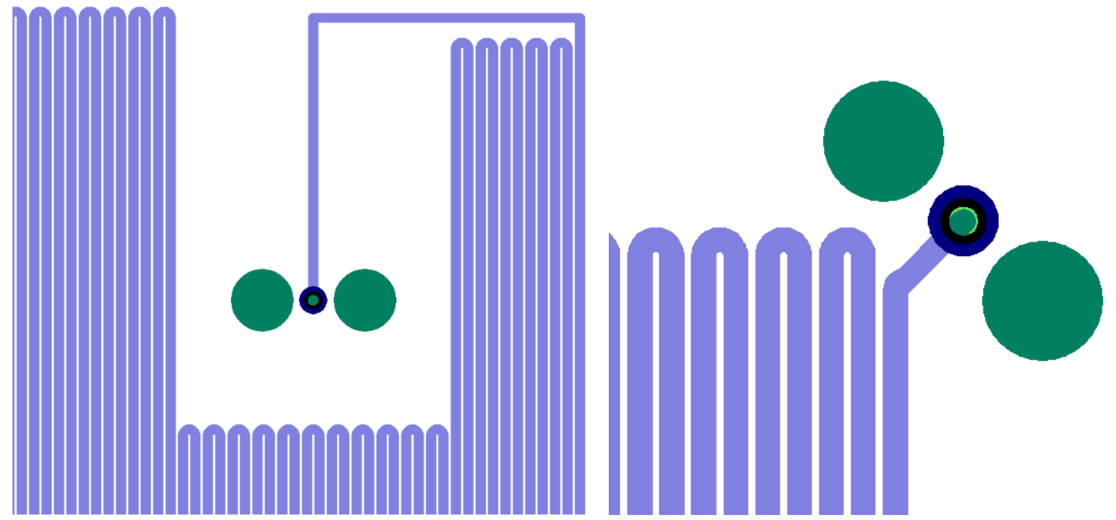

Figure 15 Smaller original outlet geometry and corner original outlet geometry with nozzles surrounding the green outlet geometries.

4.2 Photolithography

In the first process flow, eight µm of positive photoresist AZ960 was used as the masking material for later silicon etching on both sides of silicon wafers. The silicon wafers were pretreated with vapor HDMS (Hexamethyldisilazane) for better photoresist adhesion. The automatic coater EVG150 and double side mask aligner Süss MA150 at CMi were used to coat, expose and develop the photoresist. The UV lamp within the Süss MA150 had a power of 10 mW/cm^2 the photoresist was exposed four times for 5.8 seconds each within the, giving an total exposure dose of 232 mJ/cm^2. Figure 16 shows an example of good photolithography results during fabrication with the first process flow. The widths of the microcolumns and walls were approximately 120 and 40 µm, proving that there was a good translation of the mask design into the thick photoresist.

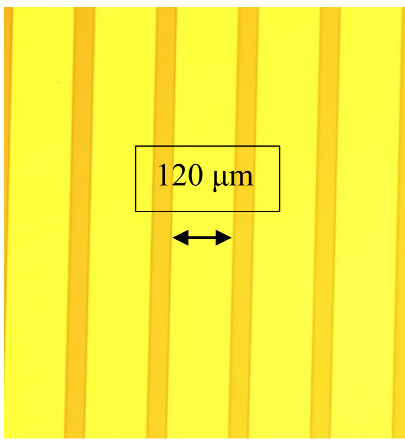

Figure 16 Example of good photolithography results during the first process flow fabrication.

Initially, the photoresist on the wafers was placed in hard contact with the masks. It was found that the hard contact caused photoresist to heat up and deposit onto the mask, dirtying the mask. Then any wafers exposed with the same mask have defects inside the structures. Some examples of photoresist defects can be seen in Figure 17. These photoresist defects would later protect the silicon surface under them from being etched and destroy the microcolumns' ability to filter.

Cleaning the masks of the photoresist took much time and usually could not be completely cleared of the defects or gather new ones during the cleaning process. When new masks were fabricated and suffered the same problems, soft contact was used in an effort to decrease the photoresist deposition on the mask. However, even this did not solve the problem completely.

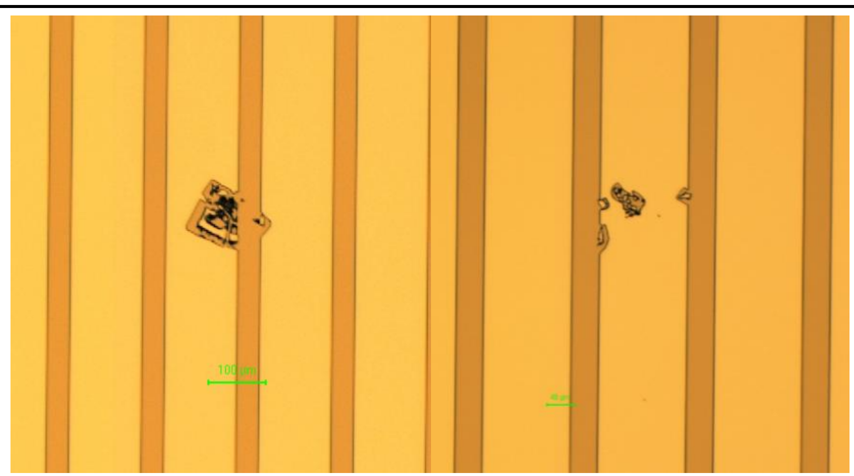

Figure 17 Defects inside the photoresist structures due to defects on the mask.

Therefore, to avoid any mask-related issues, the direct laser writer Heidelberg VPG200 was used to directly write on the photoresist coated wafers during the second process flow. The Rite Track 88 Series was used to deposit and develop 2 µm of positive photoresist ECI 3027 during the second process flow. The photoresist was exposed 5 times at an intensity of 60%. The Rite Track 88 Series was used instead of the EVG150 during the second process flow due to an decrease in the amount of defects seen inside the photoresist just after deposition. A thicker photoresist was used because this also decreased the number of defects in the photoresist after deposition. With the mask-less photolithography, the microcolumn designs translated well into the photoresist and there was no significant deviation in their dimensions.

4.3 Etching

During the first and second process flows, silicon was etched by DRIE (deep reactive ion etching) using the Alcatel AMS 200 SE or Alcatel 601E machines available at CMi. The

microcolumns were etched 200 μm deep on the topside of silicon wafers. After anodic bonding to glass to seal the microcolumns, the backsides of the silicon wafers were masked with photoresist (parameters dependent on which process flow being used), as described in the previous section, and then the exposed silicon was etched to create the inlets and outlets.

Figure 18 shows the results of the microcolumn etching with SEM (scanning electron microscope) images. The walls were very close to vertical and the difference in etching depths between the center of the microcolumn and the edge was always less than 10 μm when measured by the Veeco Wyko NY1100, an optical profiler at CMi. However, when the microcolumns were etched inside the Alcatel 601E, there was a large increase in the etching rates between the center and edge of the silicon wafer, which meant that the microcolumn chips closer to the edge of the wafer were etched 10-20 microns deeper, on average, than the center chip. Each microcolumn chip's depth was therefore measured by the optical profiler at the center of the chip and at the corner of the chip if the chips were very close to the silicon wafer edge.

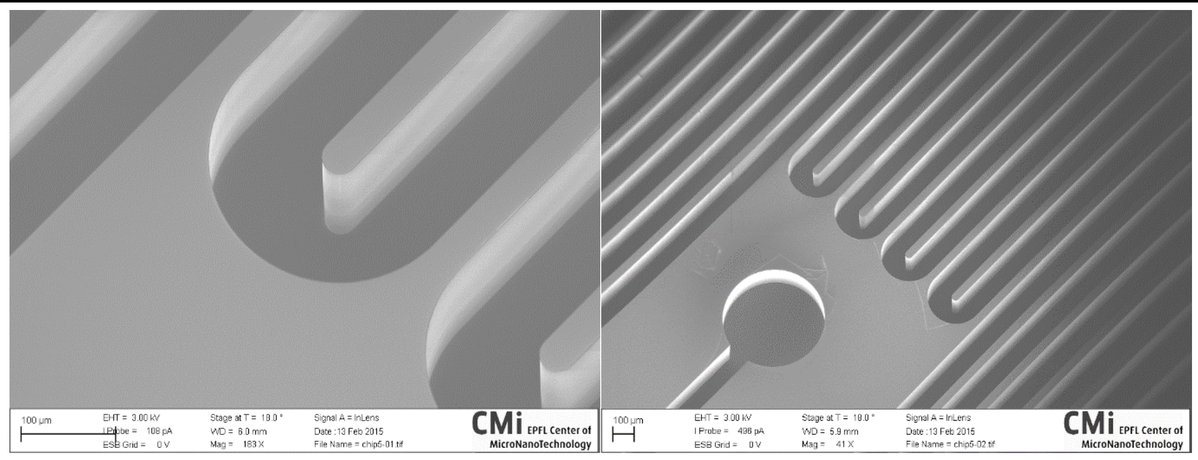

Figure 18 SEM images of results after DRIE of microcolumns. Left image is a close up of the microcolumns shown in the right image. Images courtesy of Cyrille Hibert

It was common that defects would occur during the DRIE process, in both process flows. Some SEM images of these defects can be seen in Figure 19. Their sizes ranged from a few microns to across multiple microcolumns. These defects accumulated during the DRIE process until dozens were spread across the silicon wafers inside the microcolumns. Both the Alcatel machines produced these defects and only doing a short dielectric etch step in between silicon etching steps would help correct the errors.

The most plausible explanation as to why these defects occurred is that the side walls would fall into the microcolumns because of the pacification during the etching process. When the side walls fell, they would mask the microcolumns so that the silicon would not be etched underneath. The dielectric etch step would help to etch away the fallen side walls so that the silicon could continue to be etched.

Some of the defects were present before the etching process from the photolithography and/or silicon oxide etching steps and these also turned into errors within the microcolumns. However, the number of these defects was much less than the defects accumulated during the

DRIE process. Every effort was made to cleanly process the silicon wafers before silicon etching to minimize these defects.

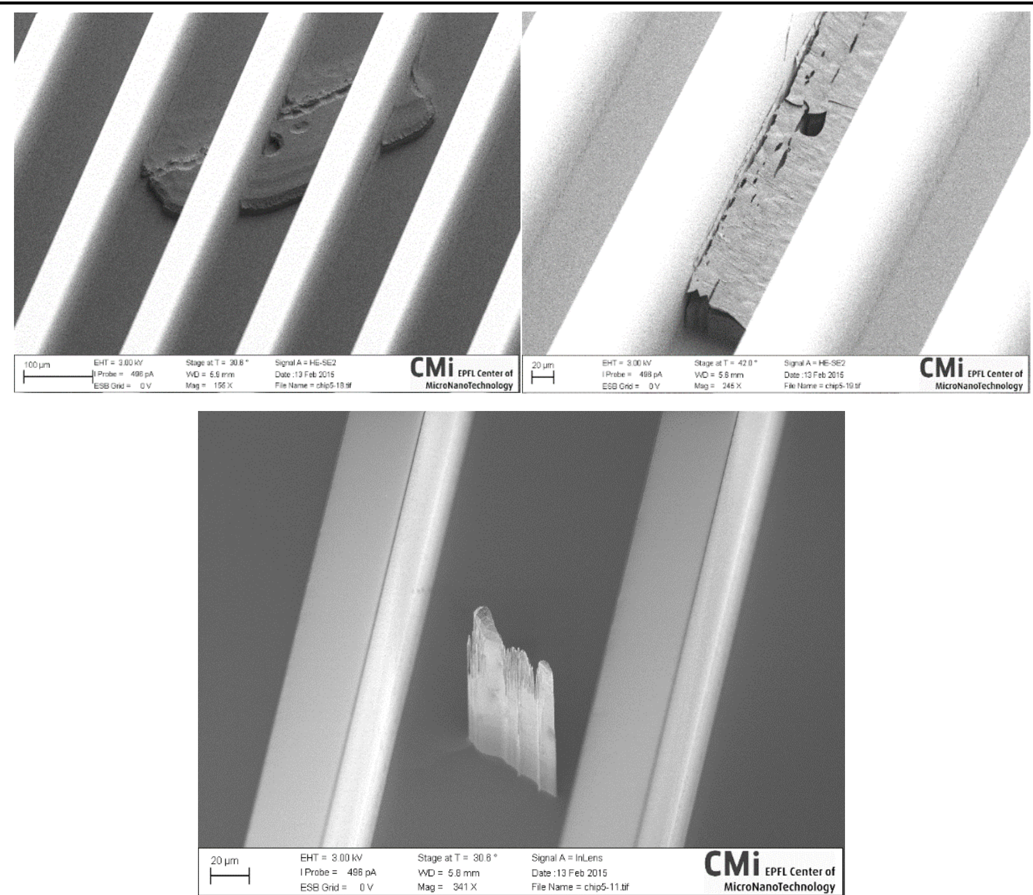

Figure 19 Defects found after DRIE inside the microcolumns. Images courtesy of Cyrille Hibert.

Silicon oxide was etched during the second process flow by dry etching with the SPTS APS Dielectric Etcher or at the Plate Oxide wet bench with BHF (buffered hydrofluoric acid). The dry etching was used to etch silicon oxide that was left exposed after photoresist had been patterned as a mask on top. The wet etching was used to strip the silicon oxide off the topsides of silicon wafers to prepare them for anodic bonding and was sometimes used to etch the inlet and outlet pattern on the backsides at the same time. Both methods of etching the silicon oxide were effective and no problems were found at this fabrication step.

4.4 SU8 Nozzle Fabrication

After anodic bonding and patterning the inlets and outlets into the silicon oxide on the backsides of the wafers, SU8 photolithography was done on the backsides of the wafers. SU8 is a negative photoresist that can be used for tall or high aspect ratio structures and adheres well to both silicon and silicon oxide. It can also survive DRIE with minimal damage, which was

necessary to complete the fabrication of the wafers. The one drawback to thick SU8 processing was the long soft baking, post exposure baking, relaxation and cooldown times.

The SU8 was deposited with the Sawatec LMS200 coater and then soft baked for 2.5 hours on the Sawatec HP401Z hot plate. The Süss MA150 double side mask aligner was used to backside align the nozzles to the microcolumn designs on the topside and the photoresist was exposed four times for 13.2 seconds for a total exposure dose of 528 mJ/cm^2. Afterwards, the wafers were baked for 3.3 hours and left overnight so the photoresist could relax. Finally, the SU8 was developed with PGMEA (Propylene glycol methyl ether acetate) for at least 20 minutes at the wet bench in Zone 13 of CMi. To fully develop the photoresist inside the SU8 nozzle structures, wafers were left inside the development fluid for as long as necessary to clear the photoresist. A microscope was used to check the progress of the development inside the nozzles.

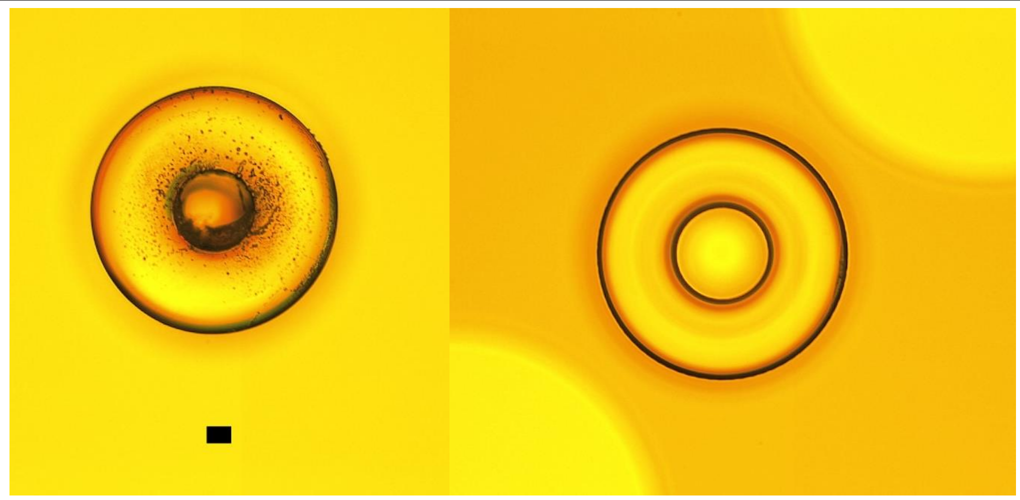

Figure 20 Left, underdeveloped and over-exposed SU8 nozzle. Right, fully developed and correctly exposed SU8 nozzle.

Some exposure tests were run to find the best exposure time. In the end, it was impossible not to have a decrease in the inner cylinder width of at least 10 µm between the top and the bottom of the nozzle. Since the SU8 nozzle would serve as the mask during the silicon etching of the outlets, it was necessary to insure that the nozzle width at the bottom of the cylinder was at least 120 µm. The nozzle mask design was altered to increase the inner cylinder width from 120 µm to 150 µm and the final fabricated nozzles were sufficiently wide enough. The average inner width of the SU8 nozzles at the top was 140 µm and 130 µm at the bottom of the nozzle. The thickness of the nozzles was approximately 110 µm.

4.5 Discussion

One wafer was completed with the first process flow, while with the second process flow seven wafers were completed. Two of these wafers had SU8 nozzles, four wafers did not have SU8 nozzles but otherwise the same outlet geometries and two wafers included corner slit outlets as seen in the first process flow masks. Each process that was done on a wafer was carefully written down in documentation that travelled with the wafers throughout the cleanroom. The location and fabrication step at which a defect was found was marked as well. All microcolumn chips had their

depths measured after the DRIE process in at least one location and all the nozzles were measured by a mechanical profiler before leaving the cleanroom.

By this careful documentation, it was possible to discover the source of some of the types of defects to minimize and/or avoid them entirely in the next iteration. However, due to time constraints, it was not possible to fully study the defects that accumulated during the DRIE process. Although one explanation has been discussed earlier, it is very possible that there are other contributions to the defects. In the future, etching tests should be completed to try to confirm that the side wall pacification is the leading cause of the defects and not possibly silicon oxide depositing into the microcolumns or inherent defects within the silicon wafers themselves.

One problem that was discovered during the dicing was that the SU8 nozzles caused a large height difference across each chip, stressing the wafers so that they broke in many pieces as the dicing saw passed over. However, since the dicing crosses were placed on the topside of the wafers, the wafers had to be taped with the nozzles pressed down and it was impossible to not have this height difference. Out of the 18 chips on the two wafers, only four microcolumn chips survived and only one chip was viable for experiments. In the future, dicing marks should be put on the backside of the wafers so that the wafers will lie flat and undergo less stress during the dicing. However, it’s possible that the nozzles could then be clogged with debris since they will be near the dicing saw and water used to dice the wafers.

One note to be made from this fabrication run is the importance of properly cleaning wafers and masks before beginning a process. Although it was sometimes difficult and time-consuming to clean thoroughly, it made a difference in the quality of the overall fabrication, particularly cleaning well at the beginning of the fabrication process. In particular, it was difficult to keep the backside of the wafers clean and undamaged during topside processing. In the future, coating the backside of the wafers with a protective layer could help reduce damage.

5. Assembly and Qualification

5.1 Experimental Setup

To test the microcolumn chips, an experimental setup was created inside the LMIS1 laboratory. The setup can be understood by the schematic shown in Figure 21. An air source provided the mobile phase to carry the sample volume through the microcolumn chip onto the gas sensor and then outside of the system. The air source was controlled by a pressure regulator to decrease the air pressure to 1.5 bar above the ambient pressure. A three-way valve controlled when a sample volume is injected into the microcolumns; unless the three-way valve was activated, air would pass continuously into the microcolumns by moving through the upper tube connected to the three-way valve. When the three-way valve was activated, air moved through the bottom tube connected to the three-way valve and carried a sample volume through the microcolumn chip.

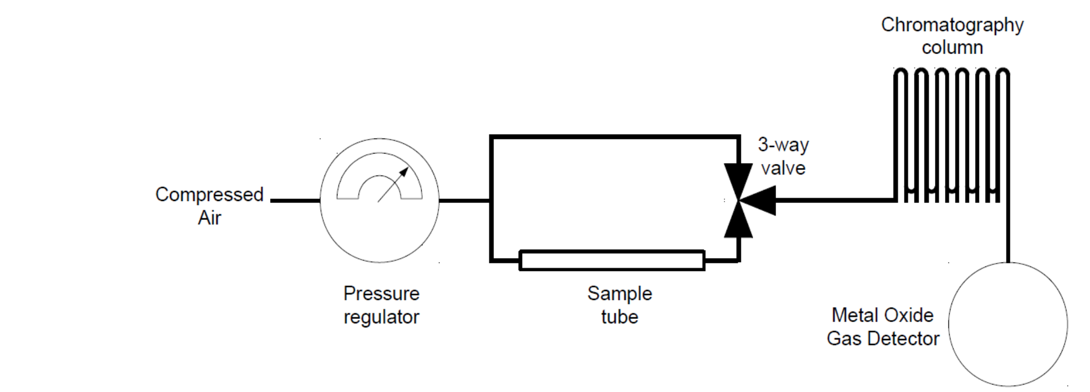

Figure 21 Schematic of the gas chromatography setup used in this master thesis, excluding the electronics. Taken from [8].

Figure 22 shows the experimental setup inside the laboratory. A stereoscope was used to align the microcolumn to the gas sensor as well as visually check the position of the microcolumn outlet in reference to the gas sensor during measurements. The power source provided power to both the gas sensor and the three-way valve. Not pictured is the compressed air source or the computer with the LabVIEW program that controlled the three-way and collected the signal from the gas sensor. The LabVIEW program also created a text file that saved the time and measured voltage for later analysis.

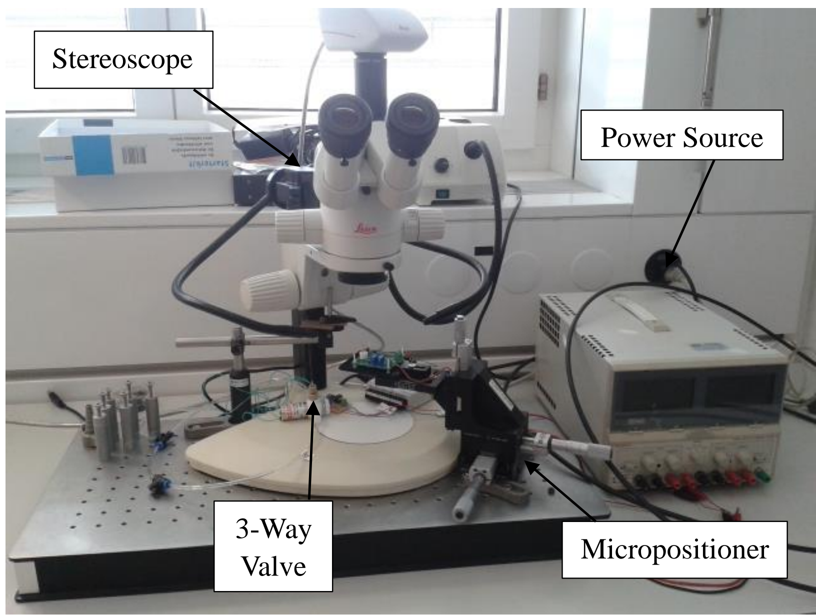

Figure 22 Experimental setup for testing the microcolumns, excluding the computer and air source.

The three-way valve was connected directly to the inlet of the microcolumns by a tube and nanoport connector. A hydraulic inlet connector was designed during this master thesis, shown in Appendix F, to hydraulically connect the microcolumn inlet and the nanoport connector and maintain the connection throughout the experiments. The microcolumn chip was held in place above the gas sensor by an arm with a clamper, shown in Figure 23. The gas sensor was connected to a PCB, which was secured onto the micropositioners and moved by the micropositioners for aligning and testing at different positions.

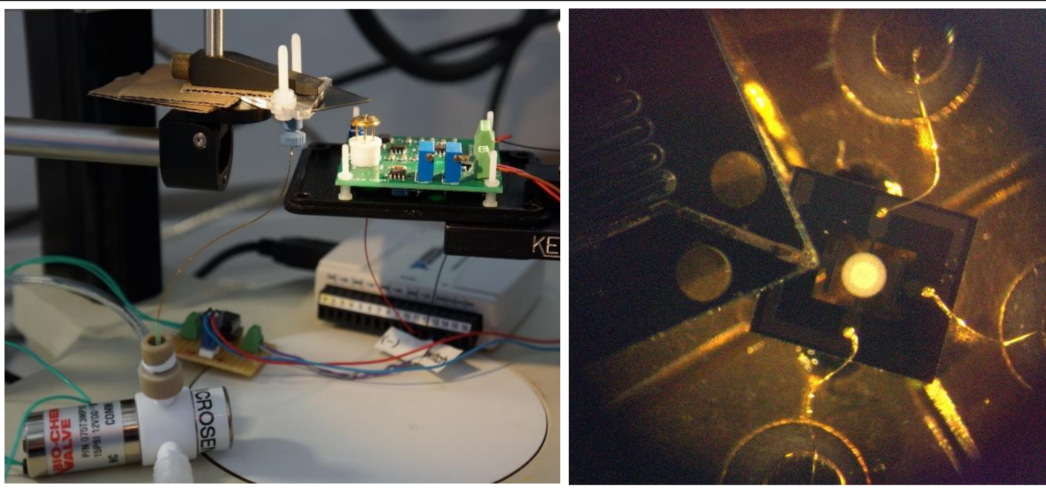

Figure 23 Right, Close-up on experimental setup. Tin-oxide gas sensor is the gold object on stilts on top of a white holder. The microcolumn is held by the arm.
Left, view through stereoscope while aligning a slit corner outlet to the active area of the gas sensor (white circle in center of black chip).

The alignment of the gas sensor to the microcolumn outlet in the z-axis was made by touching the edge of the microcolumn chip on the edge of the gas sensor chip. The point of contact was seen by using the stereoscope and little damage occurred to the gas sensor in the process. The x and y alignment was also visually controlled through the stereoscope.

A bubbler was used to create the sample volumes for experiments and contained a mixture of 1 mL ethanol to 1000 mL water, which was made fresh for each outlet tested. With this mixture, the concentration was on the order of 20 ppm. During the experiments, every position of the microcolumn outlet that was tested was given a fresh sample volume to ensure testing wasn't completed with a depleted sample volume. The injection period for the experiments was 500 milliseconds.

5.2 Measurements

Before a detailed experiment was completed on any microcolumn chips, several chips were tested by manually injecting air into the microcolumns while they were inside a beaker of water. Microcolumns that produced air bubbles at the outlets inside the water were initially considered to be working. Each of the outlet geometries fabricated, except for the nozzle on the corner outlet, were tested with the experimental setup. The modified original outlets were tested at four positions across the 300 µm wide gas sensor on the x-y plane, marked by the green circle in Figure 24. The slit corner outlet was placed at seven positions relative to the gas sensor, as seen in the left image of Figure 24, to see the influence of the slit opening on the results. In Figure 24, the red dots and purple squares denote the position of the outlet center or beginning of the slit, respectively. Each position was 100 µm from each other and At each position, three measurements were taken. Several heights above the sensor were measured during the testing of each outlet, ranging from 300 µm to 700 µm.

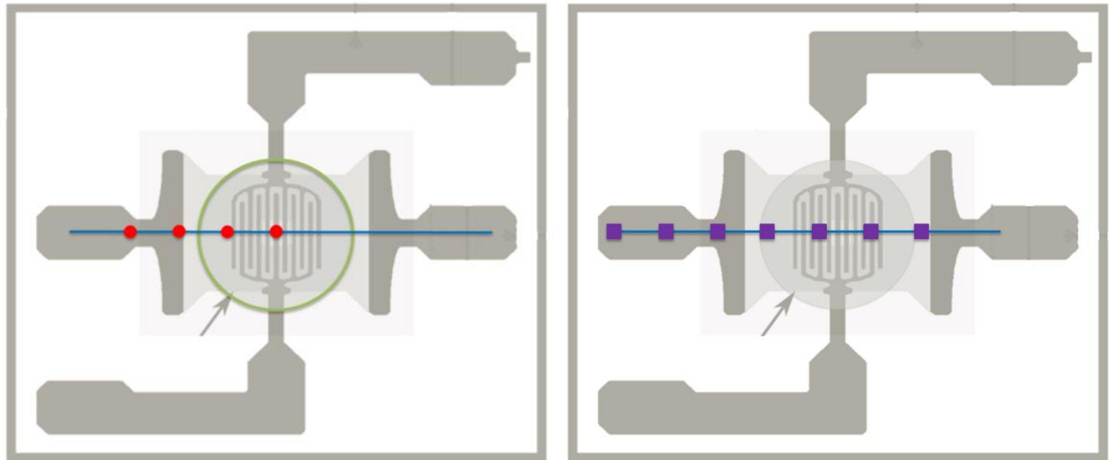

Figure 24 Right image: Diagram of tested positions, shown as red dots, of the modified original outlet across the gas sensor. The green circle encircles the active area of the gas sensor. Left image:

Diagram of tested positions of the corner side outlet with slits outlet across the gas sensor, where each purple square shows where the beginning of the slit was placed.

The gas sensor measured the ethanol in the sample given by the injections in each measurement and gave output peaks that measured in volts. To fit the output peaks and find the peak height and full width at half maximum, a MATLAB code was written by colleague Soumya Yandrapalli. Figure 25 shows an output peak fitted with a Gaussian curve. The measured peaks were asymmetric and a large tail after the peak was present. After the fitting was complete, the average of the three measurements at each position was found, as well as the standard deviation. Origin was used to plot the final results.

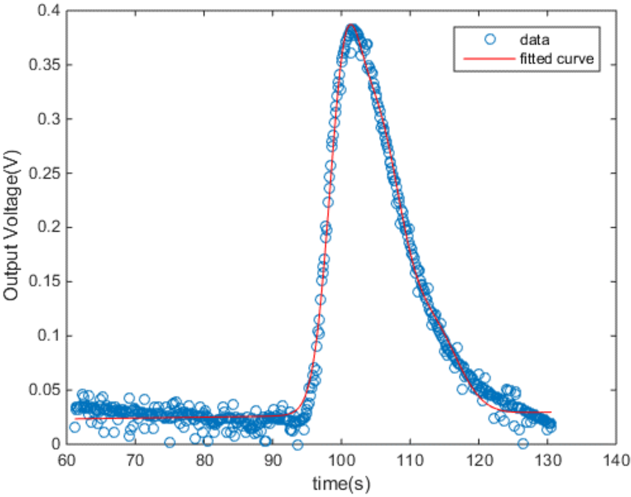

Figure 25 Example of a fitted peak from the MATLAB data analysis.

5.3 Results

The average FWHM and peak heights at each position are shown in Figure 26 and Figure 27 for the smaller original outlet. Although there is no correlation between position and the measured FWHM, there is a correlation between height above the sensor and average peak height, especially as the outlet was moved close to the sensor.

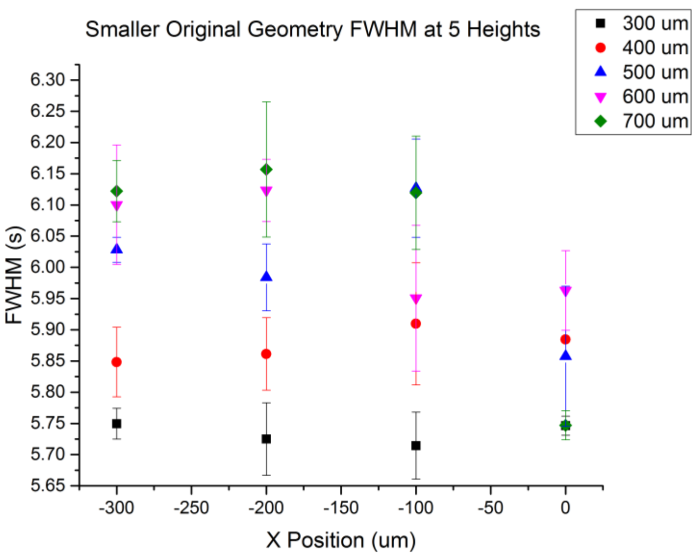

Figure 26 Smaller original geometry FWHM results.

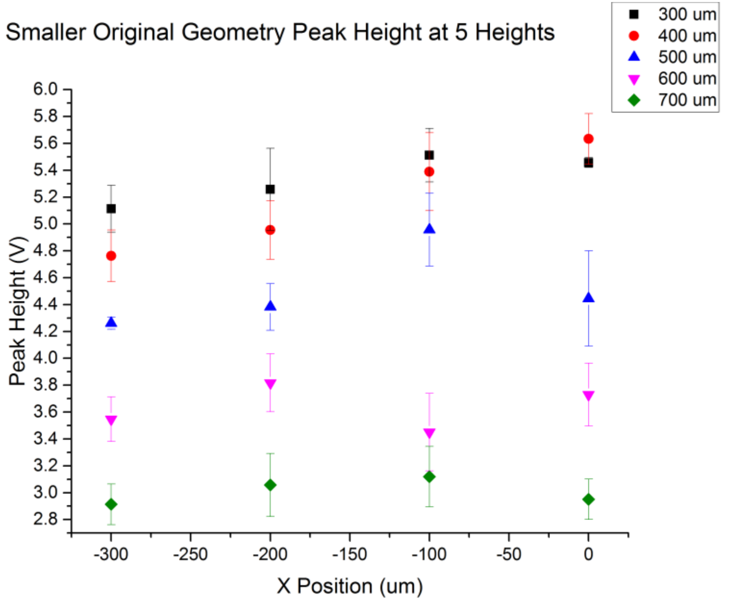

Figure 27 Smaller original geometry peak height results.

Figure 28 and Figure 29 show the FWHM and peak height results for a nozzle outlet with similar conclusions as the smaller original outlet. Since a fresh mixture was made for testing each outlet, it is not possible to compare directly the results of the smaller original outlet and the nozzle outlet. However, the general behavior of the signal is the same with these two geometries, as well as with the corner original outlet and corner side outlet with slits, whose results can be

seen in Appendix G. The corner original outlet microcolumn chip had some defects that caused the peak to be broadened relative to the other outlet results.

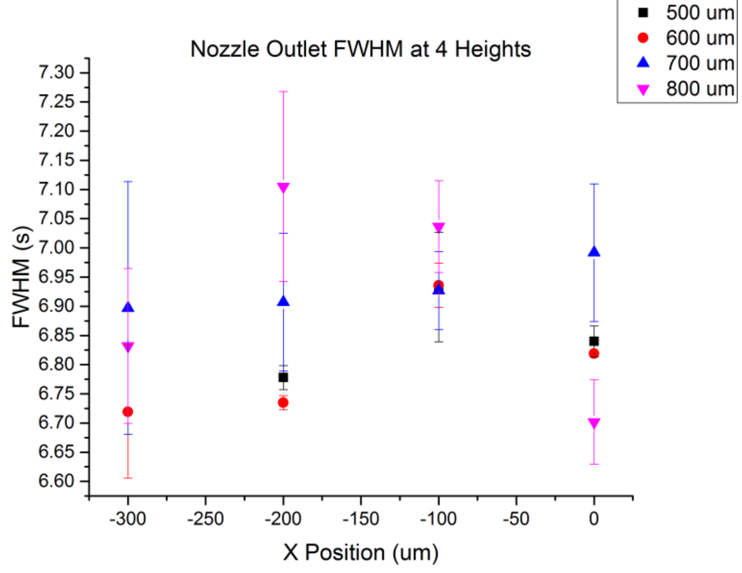

Figure 28 Nozzle Outlet FWHM results at 4 heights above the gas sensor.

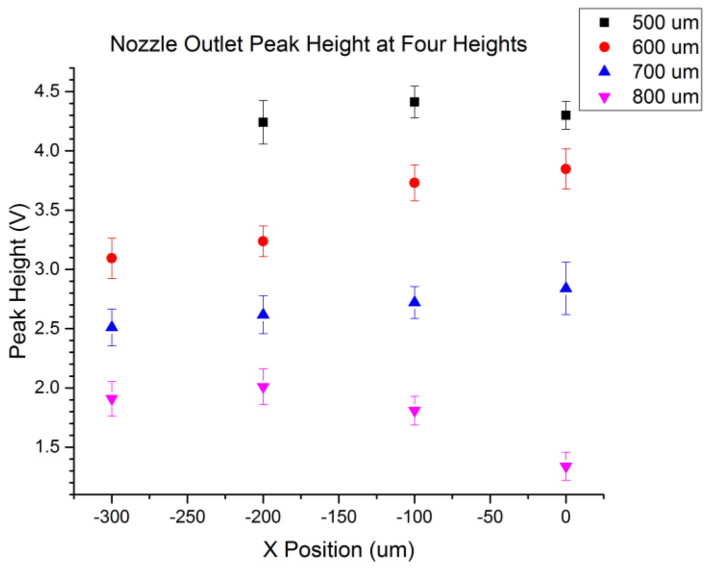

Figure 29 Nozzle Outlet peak height results at 4 heights above the gas sensor.

When the surface velocity magnitude is calculated at each position measured during the experiments and compared to the experimental results, it was found that the FWHM did not significantly change as the velocity magnitude increased or decreased. The peak height,

however, did increase as the velocity magnitude increased. Figure 30 and Figure 31 show the comparison for the smaller original outlet.

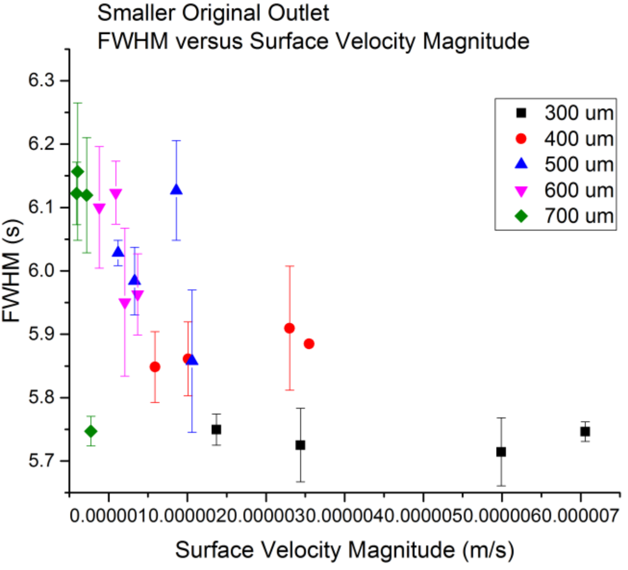

Figure 30 Smaller original outlet FWHM results versus surface velocity magnitude calculated at the corresponding position.

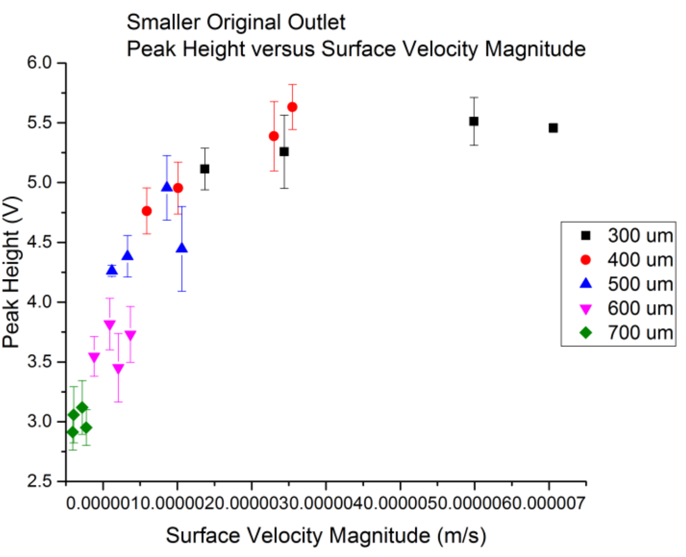

Figure 31 Smaller original outlet peak height results versus surface velocity magnitude calculated at the corresponding position.

5.3 Discussion

The results of the experiments partially confirmed the hypothesis formed by the FEA results: The signal height is influenced by the velocity of the sample when it reaches the gas sensor surface, but the FWHM is most likely controlled by another aspect of the microcolumn chip. In general, the average FWHM measured with this microcolumn chip was an order of magnitude better than the results found within the last master thesis concerning microcolumn optimization with Microsens [8]. In the previous work, the FWHM was on the order of 35 seconds, while an average of 5 seconds was measured in the experiments of this project.

However, in the previous work, the microcolumns were coated with a PDMS stationary phase, tested with a different chemical (methyl-cyclohexane) and were heated. It is unlikely that these factors could completely account for the large difference in results between the two works, but it is important that the microcolumns produced in this project also be tested with a stationary phase and the same analyte to see if there was a true improvement in the signal shape.

Although it was thought that the defects produced by the DRIE would cause many microcolumns to be blocked, only 2 out of the 19 microcolumn chips tested in water were actually blocked. This means that the defects may cause much harm than originally suspected. However, it is possible that microcolumns can allow air to pass through, but still be defected enough to not separate gases in a sample volume. A semi-blocked microcolumn chip gives a very long retention time compared to what was measured for an unblocked microcolumn chip. In the future, this may prove useful information when testing many chips and are unsure if the defects pose a significant issue to proper gas separation.

It is not possible with this setup to compare results between the different outlet designs, but it is clear that the behavior of the results is similar across the designs. Microcolumns with side outlets have not been seen in literature and they may prove effective at transporting the sample gases to the sensor and refreshing the sensor after detection. In the future, several microcolumn chips of each outlet geometry should be tested without and with a stationary phase and the same sample volume source to verify any improvements to the original outlet geometry. When it is clear which geometries were the most effective, then the FEA results can be compared to see if they showed the same geometries as effective.

6. Conclusion

The goal of this master thesis was to improve the outlet design of microcolumns and the microcolumn chip assembly to a tin-oxide resistive sensor. To that end, three simulations runs were completed with many different outlet geometries to understand the fluid dynamics between the microcolumn outlet and the gas sensor. The velocity magnitude measured near the gas sensor inside the simulation models was used as a marker of how well the outlet geometry guided the air flow onto the gas sensor. Velocity field arrow diagrams were used to understand how the air flow moved from the outlet onto the gas sensor. After studying the results of the simulation results calculated for each outlet geometry, five outlet designs were chosen to be fabricated.

Two process flows were used during the fabrication phase of the project to create eight wafers that contained many of each type of outlet geometry. Defects during photolithography and DRIE were a common issue throughout the fabrication and were minimized when possible by studying the conditions in which they occurred. The defects during photolithography tended to be due to mask contamination and particulates within the deposited photoresist. Using a direct laser writer eliminated the mask contamination problem, while switching photoresist and increasing its thickness minimized the number of particulates and their severity. For DRIE, although it could not be thoroughly studied, the explanation of defects was most plausibly side walls falling into the microcolumns due to the pacification. In the future, this issue could be avoided by brief dielectric etching steps in between silicon etching steps.

A new experimental setup was created to test the microcolumn chips, including redesigning a hydraulic inlet connector that would temporarily press a nanoport connector on the microcolumn chip inlets. The new hydraulic inlet connector put less stress on the microcolumn chips and provided an easy way to align the microcolumn inlet to the nanoport connector. In the experimental setup, the microcolumn outlet could be positioned extremely close to the gas sensor surface, thus decreasing the dead volume inside the assembly.

No stationary phase was placed inside the microcolumn chips, due to the time constraints of the project. Several microcolumn chips were initially tested by manually injecting air into the microcolumns while the chip was inside water. Even with the many defects and issues uncovered during the fabrication process, most of the chips allowed air to move all the way through the chip, decreasing fears that the defects would cripple many of the chips. Four different outlet designs were experimentally tested at several positions above the gas sensor. It was found that the measured peak heights increased as the outlet moved closer to the sensor, while the FWHM was not significantly affected by the position and is most controlled by another aspect of the microcolumn chip. This partially prove the simulation results and showed that the signal output was affected by the velocity of the sample reaching the gas sensor surface.

A variety of work was completed during this master thesis, from reading literature to understand gas chromatography with microcolumns, creating simulation models of several outlet geometries, then designing and fabricating the microcolumn chips at CMi and finally creating an experimental setup and testing the chips. The finite element analysis was useful in understanding the fluid dynamics of the microcolumn-gas sensor assembly, previously unknown. Improvements were made to the process flow for fabricating the microcolumn chips, including using a direct

laser writer to avoid photoresist defects and optimizing the fabrication of SU8 surrounding the outlets of the chips. The new experimental setup makes it possible to test within 300 µm of the surface of the gas sensor and a new hydraulic inlet connection improved the assembly of the microcolumn to the three-way valve. The results show that the signal peak height was directly influenced by the outlet position, and therefore velocity of the sample reaching the sensor and partially confirms the hypothesis formed during the FEA portion of the project. Future experiments can be conducted to prove which geometries were the most effective to fully validate the FEA models' results.

References

[1] J. Jerman, J. Angell and S. Terry, "A gas chromatographic air analyzer fabricated on a silicon wafer," *IEEE Transactions on Electronic Devices,* pp. 1880-1886, 1979.

[2] R. P. Manginell, J. M. Bauer, M. W. Moorman, L. J. Sanchez, J. M. Anderson, J. J. Whiting, D. A. Porter, D. Copic and K. E. Achyuthan, "A Monolithically-Integrated μGC Chemical Sensor System," *Sensors,* vol. 11, no. 7, pp. 6517-6532, 2011.

[3] W. R. Collin, G. Serrano, L. K. Wright, H. Chang, N. Nuñovero and E. T. Zellers, "Microfabricated Gas Chromatograph for Rapid, Trace-Level Determinations of Gas-Phase Explosive Marker Compounds," *Analytical Chemistry,* vol. 86, no. 1, pp. 655-663, 2013.

[4] A. J. Grall, E. T. Zellers and R. D. Sacks, "High-Speed Analysis of Complex Indoor VOC Mixtures by Vacuum-Outlet GC with Air Carrier Gas and Programmable Retention," *Environmental Science Technology,* vol. 35, no. 1, pp. 163-169, 2001.

[5] J. Whiting and R. Sacks, "Programmable Selectivity for GC with Series-Coupled Columns Using Pulsed Heating of the Second Column," *Analytical Chemistry,* vol. 75, no. 10, pp. 2215-2223, 2003.

[6] J. Sun, D. Cui, H. Cai, X. Chen, L. Zhang and H. Li, "Design, Modeling, Microfabrication and Characterization of the Micro Gas Chromatography Columns," in *Advanced Gas Chromatography - Progress in Agricultural, Biomedical and Industrial Applications*, InTech, 2012, pp. 51-66.

[7] J. Sun, D. Cui, X. Chen, L. Zhang, H. Cai and H. Li, "Fabrication and characterization of microelectromechanical systems-based gas chromatography column with embedded micro-posts for separation of environmental carcinogens," *Journal of Chromatography A,* vol. 1291, pp. 122-128, 2013.

[8] A. Peters, "Detection of volatile organic compounds in air with a micro-fabricated gas analyzer," EPFL, 2013.

[9] V. Matei, C. Iulian and A.-F. Borcea, "Stationary Phases," in *Advanced Gas Chromatography - Progress in Agricultural, Biomedical and Industrial Applications*, Rijeka, Croatia, InTech, 2012, pp. 27-50.

[10] S. Zmapolli, I. Elmi, S. Nicoletti, L. Dori and G. Cardinali, "Selectivity enhancement of metal oxide gas sensors using a micromachined gas chromatographic column," *Sensors and Actuators B: Chemical,* vol. 105, no. 2, pp. 400-406, 2005.

[11] B. Mitrevski and P. J. Marriott, "Novel Hybrid Comprehensive 2D − Multidimensional Gas Chromatography for Precise, High-Resolution Characterization Multicomponent Samples," *Analytical Chemistry,* vol. 84, no. 11, p. 4837−4843, 2012.

[12] C. Wang, L. Yin, L. Zhang, D. Xiang and R. Gao, "Metal Oxide Gas Sensors: Sensitivity and Influencing Factors," *Sensors,* vol. 10, no. 3, pp. 2088-2106, 2010.

[13] R. L. Grob and E. F. Barry, "2.3.1 Plate Theory," in *Modern Practices of Gas Chromatography*, John Wiley & Sons, 2004, pp. 44-45.

[14] C. C. Wong, D. R. Adkins, G. C. Frye-Mason, M. L. Hudson, R. Kottenstette, C. M. matzke, J. N. Shadid and A. G. Salinger, "Modeling transport in gas chromatography columns for the MicroChemLab," in *SPIE Conference on Microfluidic Devices and Systems II*, Santa Clara, California, 1999.

[15] H. Shea and P. Renaud, "Chapter V: Fluidics," Scaling in MEMS, EPFL, 2014.

[16] J. S. Bunch, S. S. Verbridge, J. S. Alden, A. M. van der Zande, J. M. Parpia, H. G. Craighead and P. L. McEuen, "Impermeable Atomic Membranes from Graphene Sheets," *Nano Letters,* vol. 8, no. 8, pp. 2458-2462, 2008.

Appendix A

1.5 by 1.5 by .2 mm^3, velocity magnitude slice 10 μm above sensor

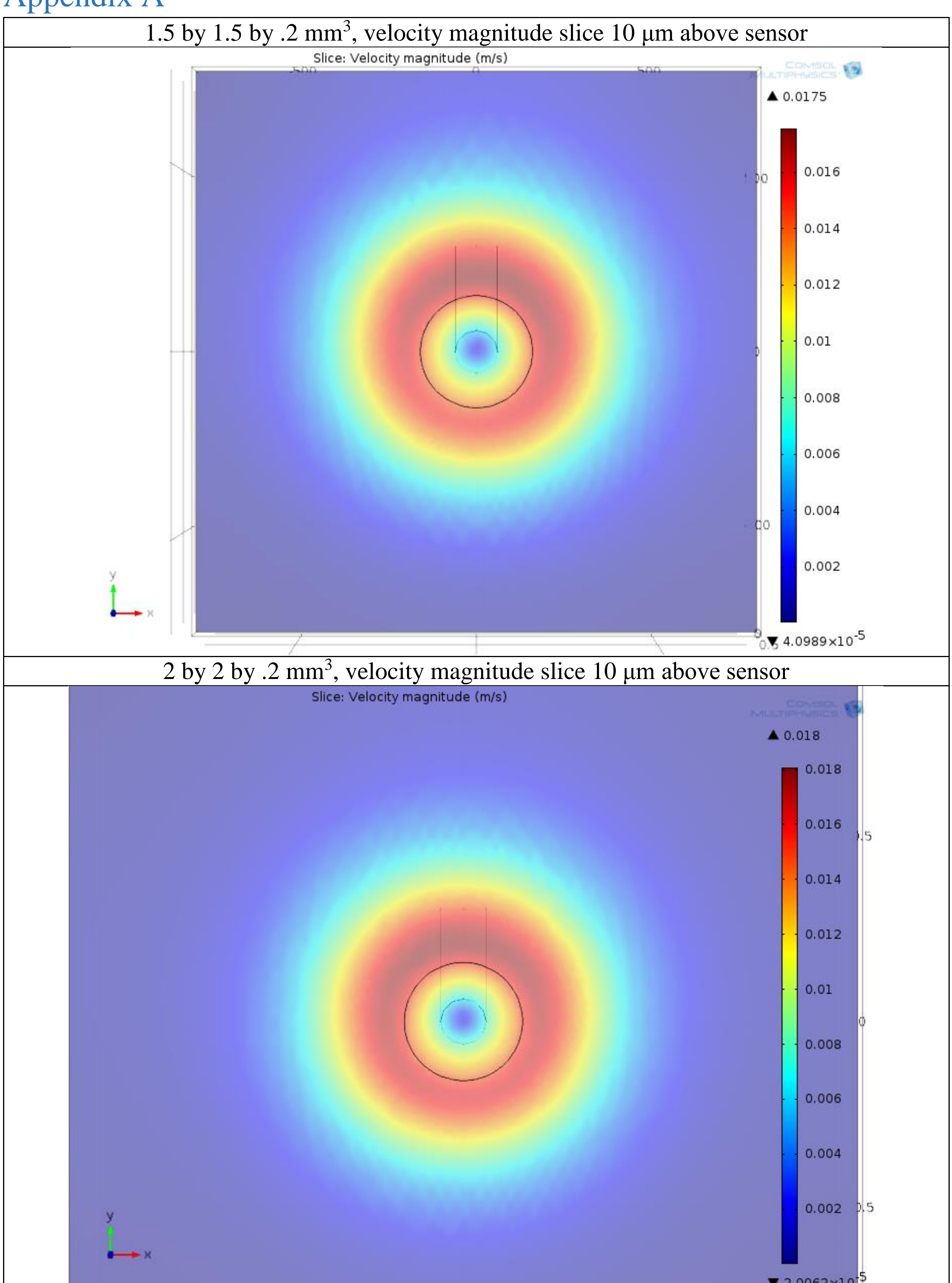

2 by 2 by .2 mm^3, velocity magnitude slice 10 μm above sensor

3 by 3 by .2 mm^3, velocity magnitude slice 10 μm above sensor

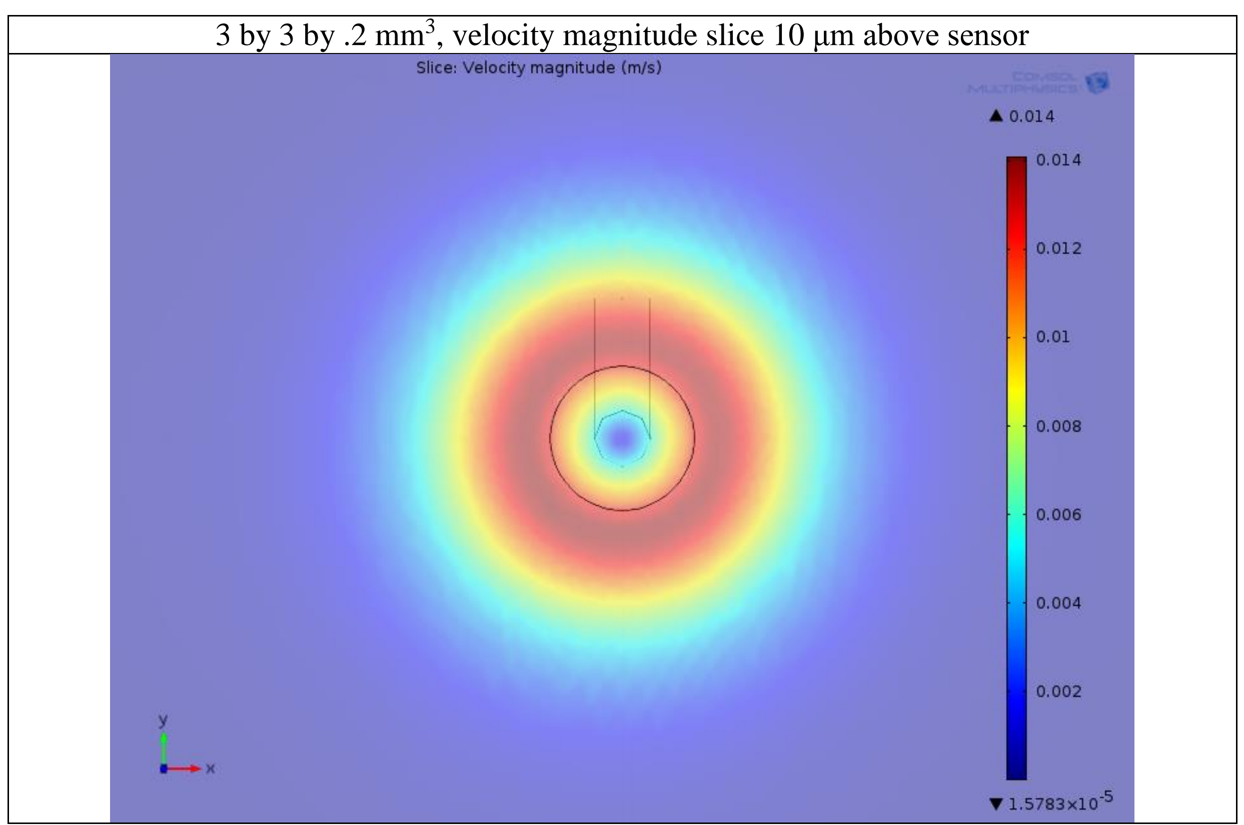

Appendix B

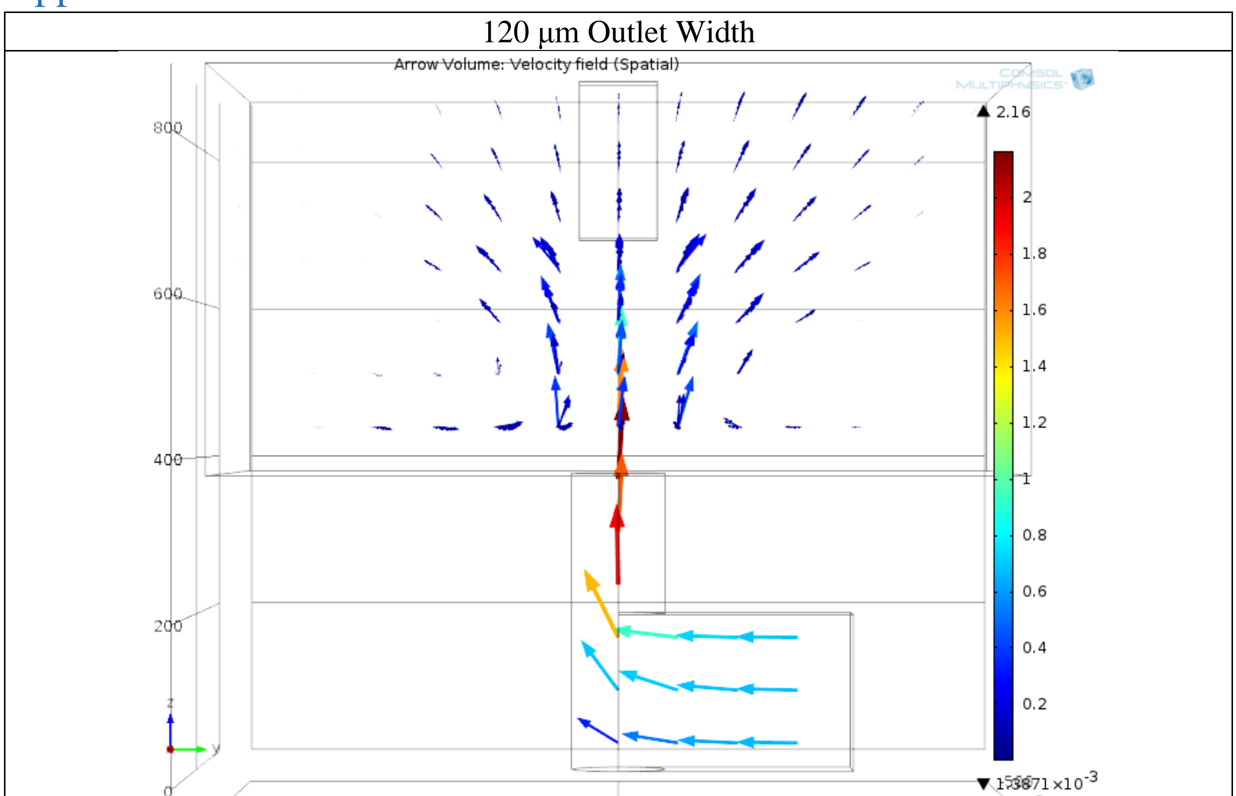

Appendix C

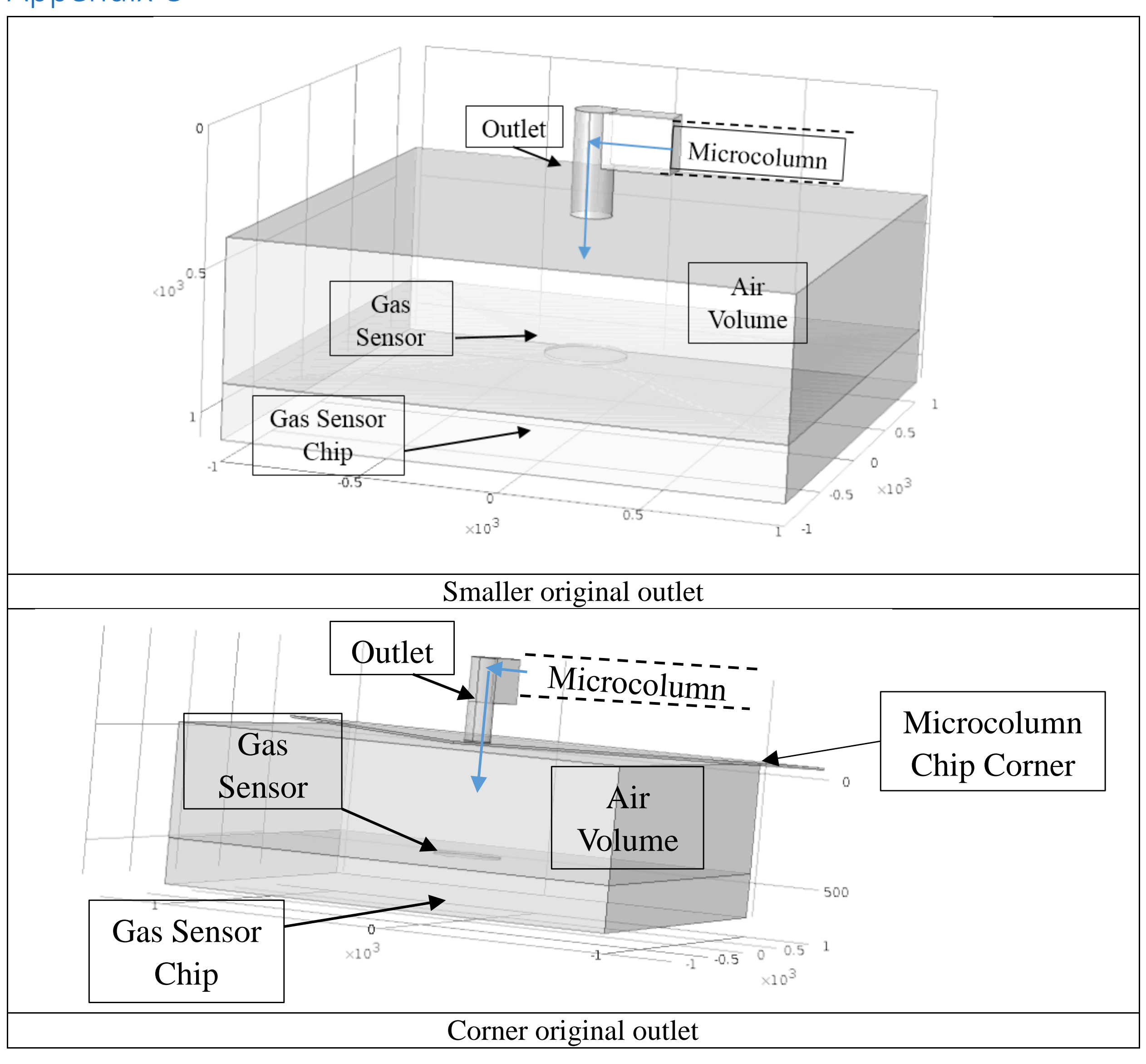

Smaller original outlet

Corner original outlet

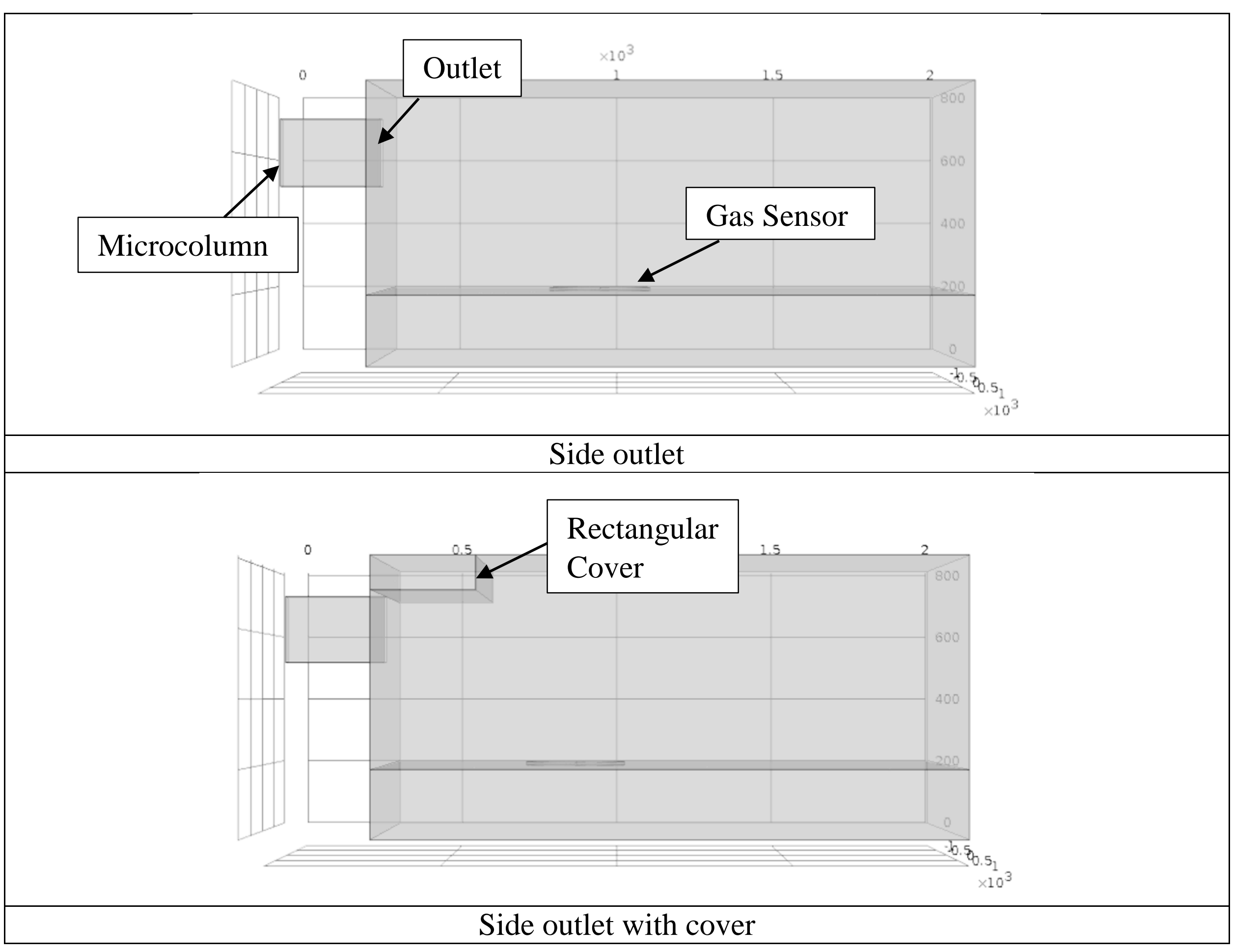

Side outlet
Side outlet with cover

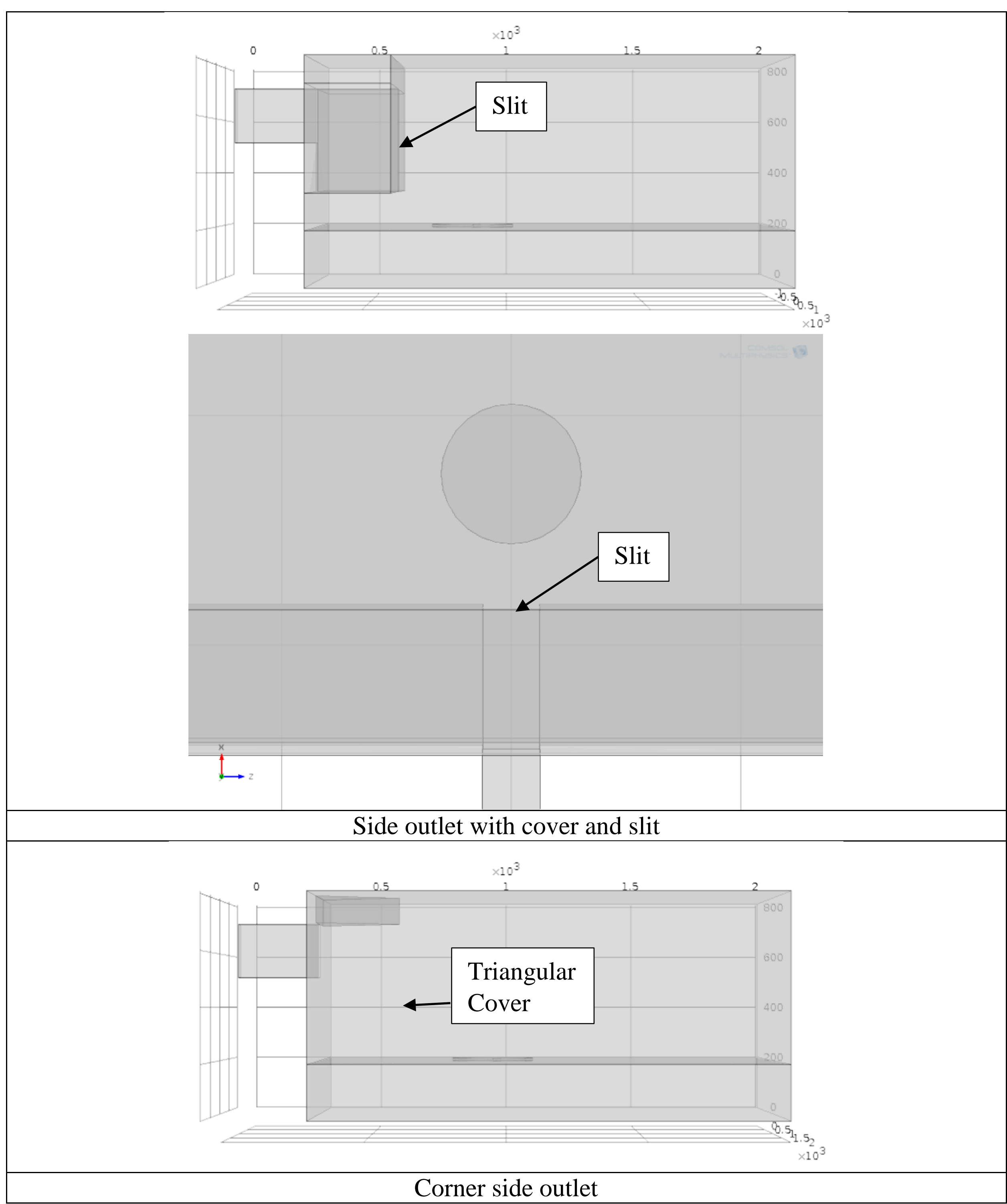

Side outlet with cover and slit

Corner side outlet

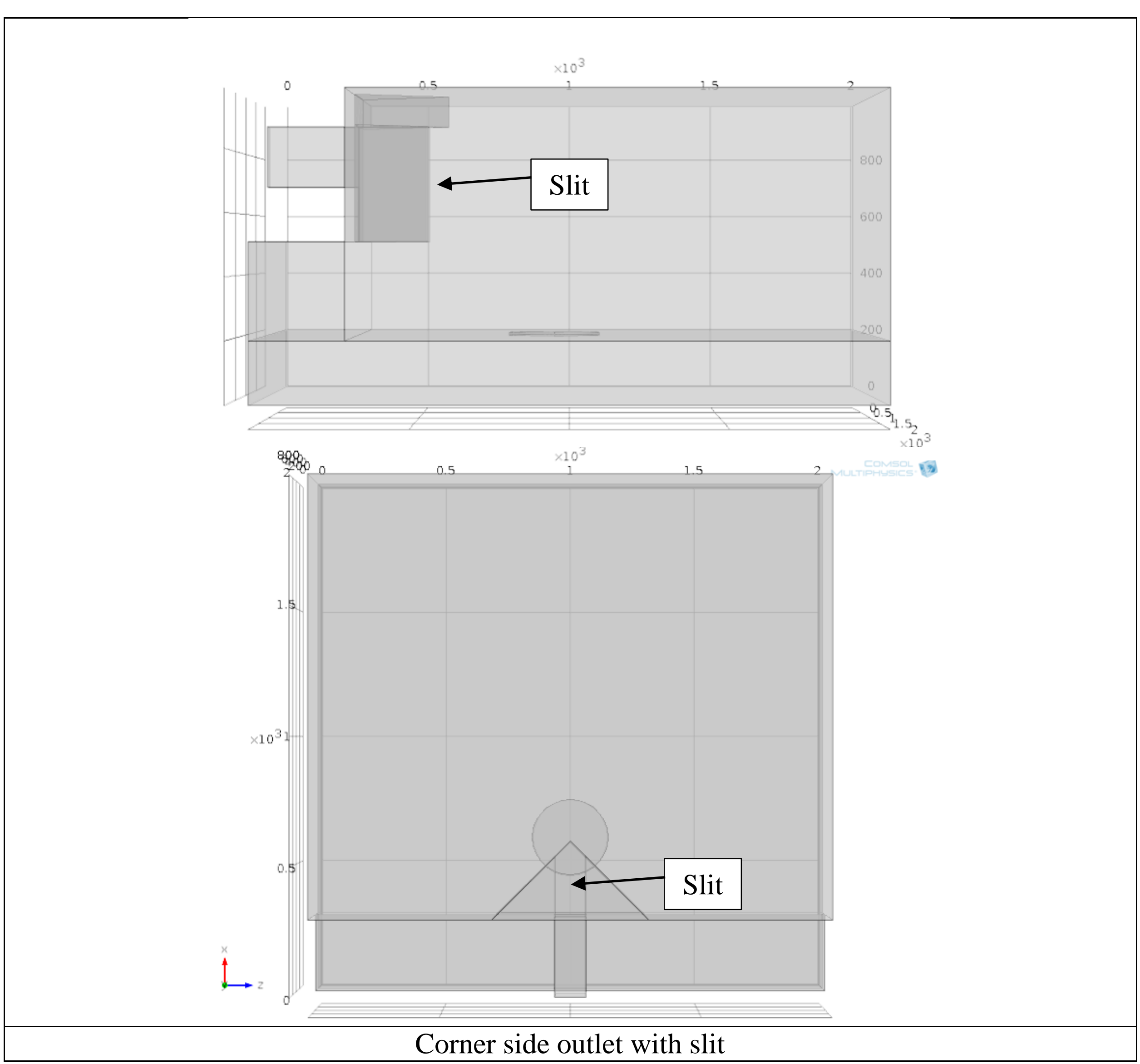

Corner side outlet with slit

Appendix D

The goal is to find the change in frequency of a membrane due to an elongation from differential pressure. First, we are interested in finding the elongation of a membrane with a certain size due to a certain differential pressure. We start with [16]:

$$\Delta p = \frac{4z}{a^2}(c_1 S_0 + \frac{4c_1 Etz^2}{a^2(1-\nu)}) \tag{5}$$

Where z is the maximum deflection, a is one half of the side of a square membrane, c_1 and c_2 are constants determined by the material, S_0 is the initial tension found in the material before deformation, E is the Young's Modulus, t is the thickness of the membrane and ν is the Poisson's ratio. In our region of interest ($5e^{-6}$-$5e^{-5}$ m for size of membrane) , there is a linear relationship between the differential pressure and deflection. Therefore, the above formula can be simplified to the one below:

$$\Delta p = \frac{4z}{a^2}(c_1 S_0) \tag{6}$$

Solving for z, we find that:

$$z = \frac{\Delta p a^2}{4c_1 S_0} \tag{7}$$

The frequency of a resonating membrane is determined by the following formula:

$$f = \sqrt{\frac{\sigma}{\rho}}\left(\frac{1}{L}\right) \tag{8}$$

Where σ is the stress inside the material, ρ is the density of the material and L is the length of the structure. When the above equation is Taylor expanded about the length, it is found that:

$$\delta f = \sqrt{\frac{\sigma}{\rho}}\left(\frac{1}{L}\right)\left(-\frac{\delta L}{L_0}\right) \rightarrow \frac{\delta f}{f} = -\frac{\delta L}{L_0} \tag{9}$$

The elongation of the membrane due to the differential pressure can be approximated by the following:

$$\delta L \sim \frac{z^2}{L_0} \tag{10}$$

Finally, combining Equations 3 and 6 into Equation 5:

$$\frac{\delta f}{f} = -\frac{z^2}{L_0^2} = -\left(\frac{\Delta p a^2}{4c_1 S_0}\right)^2 \cdot \frac{1}{L_0^2} = -\left(\frac{\Delta \mathrm{pa}}{8c_1 S_0}\right)^2 \approx -\frac{1}{100}\left(\frac{\Delta P}{\sigma_0} \cdot \frac{L}{t}\right)^2 \quad (11)$$

$$\frac{\delta f}{f} = -\left(\frac{1}{16 * 3.4}\frac{\Delta P}{\sigma_0} \cdot \frac{L}{t}\right)^2$$

L_0 is equal to 2a. The first part of Equation 7 is an approximation while the second part of Equation 7 is with the correct constants 16 and 3.4 in the denominator.

Below are the results for membranes with side lengths between 1 μm and 50 μm, with a sigma of 10 MPa and thickness of .3 nm:

a (m)	**5.00E-07**	**2.50E-06**	**5.00E-06**	**1.00E-05**	**2.50E-05**	**5.00E-05**
Δp (Pa)	**df/f**	**df/f**	**df/f**	**df/f**	**df/f**	**df/f**
0.001	3.75E-17	9.39E-16	3.75E-15	1.50E-14	9.39E-14	3.75E-13
0.01	3.75E-15	9.39E-14	3.75E-13	1.50E-12	9.39E-12	3.75E-11
0.1	3.75E-13	9.39E-12	3.75E-11	1.50E-10	9.39E-10	3.75E-09
1	3.75E-11	9.39E-10	3.75E-09	1.50E-08	9.39E-08	3.75E-07
10	3.75E-09	9.39E-08	3.75E-07	1.50E-06	9.39E-06	3.75E-05
100	3.75E-07	9.39E-06	3.75E-05	1.50E-04	9.39E-04	3.75E-03
1000	3.75E-05	9.39E-04	3.75E-03	1.50E-02	9.39E-02	3.75E-01

Using Equation 7, the deflection is calculated for various values of differential pressure:

a (m)	**5.00E-07**	**2.50E-06**	**5.00E-06**	**1.00E-05**	**2.50E-05**	**5.00E-05**
Δp (Pa)	**z (m)**	**z (m)**	**z (m)**	**z (m)**	**z (m)**	**z (m)**
0.001	6.14E-15	1.54E-13	6.14E-13	2.46E-12	1.54E-11	6.14E-11
0.01	6.14E-14	1.54E-12	6.14E-12	2.46E-11	1.54E-10	6.14E-10
0.1	6.14E-13	1.54E-11	6.14E-11	2.46E-10	1.54E-09	6.14E-09
1	6.14E-12	1.54E-10	6.14E-10	2.46E-09	1.54E-08	6.14E-08
10	6.14E-11	1.54E-09	6.14E-09	2.46E-08	1.54E-07	6.14E-07
100	6.14E-10	1.54E-08	6.14E-08	2.46E-07	1.54E-06	6.14E-06
1000	6.14E-09	1.54E-07	6.14E-07	2.46E-06	1.54E-05	6.14E-05

Appendix E

Project : GraphGas
Operator : Kaitlin Howell
Created : 08.10.14 **Last revision** : 13.10.14
Substrates : silicon <100>, 100mm, 380um, double side; Borofloat 33, 100mm, 500um, Single Side

Step N°	Description	Equipment	Program / Parameters	Target	Actual	Remarks	Name	Date
0	**WAFER PREPARATION**							
0.1	Stock out					Si, Borofloat, masks		
0.2	Check							
0.3	Clean	Piranha						
1	**PHOTOLITHOGRAPHY - Mask 1**							
1.1	HMDS	Z6/YES3	Prog. 1					
1.2	AZ 9260 coating	Z6/ EVG150	AZ_9260_5to14um_std_5_5.php, Coat_AZ9260_8um_NoEBR	8 um	8.1+/-.3			
1.3	PR bake	Z6/ EVG150	AZ_9260_5to14um_std_5_5.php, Coat_AZ9260_8um_NoEBR					
1.4	PR expose	Z6/MA6	First mask, HC, Cl1, 232 mJ/cm2	4*5.8s,wait 10s		multi-exposure		
1.5	PR develope	Z6/ EVG150	AZ_9260_5to14um_std_5_3.php, SprayDev_8um_AZ9260					
1.6	SRD	Z2/Pirahna Bench						
1.7	Inspection	Z6/uScope	Resolution and alignment					
1.8	Descum	Z2/Tepla GiGAbatch or Z15/Tepla 300	Descum O2, Low Power, 30 sec					
2	**DRIE**							
2.1	Si DRIE	Z2/Alcatel 601E/AMS 200	Si_ambiant1	200 um	~1 hr			
2.2	Remover 1165	Z2/WB_PR_Strip	Bath 1 : main remover	15min, 70°C				
2.3	Remover 1165	Z2/WB_PR_Strip	Bain 2 : clean remover	15min, 70°C				

2.4	Fast fill rinse	Z2/WB_PR_Strip	DI Rinse					
2.5	Trickle tank	Z2/WB_PR_Strip	DI Rinse					
2.6	Spin Rinser Dryer	Z2/Semitool SRD	prog 1					
2.7	Pirahna	Z2/Pirahna Bench						
2.8	Inspection	Z6/uScope						
3	**ANODIC BONDING**							
3.1	Borofloat roughening	Z11/DAG810				for 2nd borofloat wafer		
3.2	Anodic Bonding	Z6/Suss SB6	900V, 14 %?					
3.3	Descum	Z2/Tepla GiGAbatch	Descum O2, 1min					
4	**PHOTOLITHOGRAPHY - Mask 2 BACKSIDE**							
4.1	HMDS	Z1/YES3	Prog. 0					
4.2	AZ 9260 coating	Z6/ EVG150	AZ_9260_5to14um_std_5_3.php	8 um	8.1+/-.3			
4.3	PR bake	Z6/ EVG150	AZ_9260_5to14um_std_5_3.php					
4.4	PR expose	Z6/MA6	2nd mask, HC, Cl1, 232 mJ/cm2	4*5.8s,wait 10s		multi-exposure		
4.5	PR develope	Z6/ EVG150	AZ_9260_5to14um_std_5_3.php					
4.6	PR postbake	Z6/ EVG150	AZ_9260_5to14um_std_5_3.php					
4.7	Spin Rinser Dryer	Z2/Semitool SRD	prog 1					
4.8	Inspection	Z6/uScope	Resolution and alignment					
4.9	Descum	Z2/Tepla GiGAbatch	Descum O2, 1min					
5	**DRIE 2 BACKSIDE**							
5.1	Si DRIE	Z2/Alcatel 601E	Si_ambiant1	180 um	~200 um			
5.2	Plasma O2 clean	Z2/Tepla GiGAbatch	O2 , 20 min					
5.3	Inspection	Z6/uScope						
6	**PACKAGING**							
6.1	Dicing	Disco DAD321						

Projet : GraphGas 2nd Process Flow
Operator : Kaitlin Howell
Created : 08.12.14 **Last revision** : 11.2.15
Substrates : silicon <100>, 100mm, 380um, double side, 1.5 um wet oxide; Borofloat 33, 100mm, 500um, Double Side

Step N°	Description	Equipement	Program / Parameters	Target	Time	Remarks
0	**WAFER PREPARATION**					
0.1	Stock out					Si, Borofloat, masks
0.2	Check					Clean if not directly from RCA
1	**PHOTOLITHOGRAPHY - Mask 1**					
1.1	HMDS	Z6/YES3 or Z1/YES3	Prog. 1 or 5		30 min	Push door until vacuum reached
1.2	ECI Spin and Bake	Z1/ Rite Track	ECI no EBR 2 um, 2 dummy wafers	2 um	5 min per	wafers are pulled from bottom to top but returned top to bottom
1.3	PR Expose	Z5/VPG	Intensity 60%*5 sweeps		25 min per	Remember to expose wafers that were coated first
1.4	PR Develop	Z1/ Rite Track	Dev ECI 2 UM, 2 dummy wafers		5 min per	Make sure all resist developed away
1.5	SRD	Z2/Pirahna Bench	Program 1		5 min	Do immediately after development to avoid scum on backside
1.6	Inspection	Z6/uScope	Resolution and alignment		5 min per	
				Total:	52 min	Without inspection, inspection 5-10 min per wafer
Wait at least 1 hr to let wafers completely dry and relax after SRD						
2	**Oxide Etch + PR Strip**					
2.1	Oxide Etch	SPTS	SiO2 PR 2:1	1 um	4 min 10s	
2.2	Dry Resist Strip	Z2/Tepla Gigabatch	Strip_High_30s		30 s	
2.3	Wet Resist Strip	Z2/UFT Remover			15 min	Leave in cleanbath longer if not gone
2.4	Dry Resist Strip	Z2/Tepla Gigabatch	Strip_High_2min		1 min	
	Wet Oxide Etch	Z2/Plate Oxide	30s		30s	
2.5	Inspection	Z6/uScope & Z3/Nanospec			5 min per	Ensure all oxide gone in channels, no PR
				Total:	45 min	Without inspection, inspection 5-10 min per wafer
3	**DRIE**					
3.1	Si DRIE	Z2/AMS 200	Soi_accurate++	200 um	61 min	20'+20'+21'

3.2	O2 Descum	Z2/Tepla Gigabatch	High 2 min		2 min	
3.3	Piranha	Z2/Pirahna Bench			15 min	
3.4	Inspection	Z6/uScope & Z15/Wyko			~15 min	
				Total:	92 min	
4	**PR Backside Deposition Mask 2 Backside**					
4.1	HDMS	Z6/YES3 or Z1/YES3	Prog. 1 or 5		25 min	Push door until vacuum reached
4.2	PR Backside Coating	Z6/RC8 THP	AZ1512, open, 30*10 rpm, 5 acc, 30s; close, 300*10 rpm, 5*100 rpm, 30s	1.5 um	1 min	Double check all values in program before beginning! Program in notebook
4.3	PR Backside Baking	Z6/RC8 THP	Temperature <115C		1.5 min	
4.4	PR Backside Exposure	Z6 MA6	SC, 4 s		4 s	Backside alignment
4.5	PR Backside Development	Z6/ Misc Bench	AZ 726 MIF base then water then rinsing		45 s, 1 min	Slowly move the beakers in a circle to circulate the fluids.PR up!
4.6	SDR	Z2/Piranha Bench			5 min	
4.7	Inspection	Z6/uScope	Resolution and alignment		5 min per	
				Total:	40 min	
5	**Oxide Stripping/Backside Etching + PR Stripping**					
5.1	Oxide Stripping/Backside Etching	Z2/Oxide Etch	BHF		>18 min	Must double check necessary time
5.2	Wet Resist Strip	Z2/UFT Bench	1165 Technistrip		15 min	
5.3	Dry Resist Strip	Z2/Tepla GiGAbatch			1 min	
5.4	Pirahna	Z2/Piranha Bench			15 min	also piranha rough and smooth glass wafers for bonding
5.5	Inspection	Z6/uScope				
				Time:	51 min	
5	**ANODIC BONDING**					
5.1	Anodic Bonding	Z6/Suss SB6	Py_SiPy_350_lowstress_khowell		45 min	Double check T = 400C, time of voltage, watch the IV curve
5.2	Descum	Z2/Tepla GiGAbatch	Descum O2, 1min high		1 min	silicon backside to O2 plasma
8	**PHOTOLITHOGRAPHY - Mask 3 BACKSIDE - SU-8**					
8.1	Wafer preparation	Z011 / Tepla 300	Prog. 5		7 min	Not necessary if directly after previous step

8.2	Coating	Z13 / Sawatec Coater	Segment 1: Time: 5s / Speed: 500rpm Segment 2: Time: 5s / Speed: 500rpm Segment 3: Time: 5 s / Speed: 1028rpm Segment 4: Time: 40s / Speed: 1028rpm Segment 5: Time: 1s / Speed: 2028rpm Segment 6: Time: 1s / Speed: 1028rpm Segment 7: Time: 5s / Speed: 1028rpm Segment 8: Time: (1028/100)s / Speed: 0rpm End Seg		72 s	Use the "CMISTART" recipe. Use the "**Z13 Summary**" sheet to determine the speed.
8.3	Softbake	Z13 / Sawatec Hotplate on left side	Segment 1: Time: 1800-3600 s / Temp.: 30°C Base Temp.: 30°C / Vaccum : ON (Relaxation Step) Segment 2: Time: 3000 s / Temp.: 130°C End segment: OFF / Vaccum : OFF Segment 3: Time: 1200 s / Temp.: 130°C End segment: OFF / Vaccum : OFF Segment 4: Time: 3000 s / Temp.: 30°C End segment: ON / Vaccum : OFF		2.5 hr	
8.4	Exposure	Z6 / MA6	Exp. Time: 52.8 s (with 10.0 mW/cm2, mode CI1) Dose 528 mJ/cm2, SC Alignment Gap: 30	13.2s*4, 10s rest	5 min per	

8.5	Post-exposure bake	Z13 Sawatec Hotplate on right side	Segment 1: Time: 10 s / Temp.: 30°C Base Temp.: 30°C / Vaccum : ON Segment 2: Time: 3000 s / Temp.: 90 °C End segment: OFF / Vaccum : OFF Segment 3: Time: 1800 s / Temp.: 90 °C End segment: OFF / Vaccum : OFF Segment 4: Time: 1800 s / Temp.: 90 °C End segment: OFF / Vaccum : OFF Segment 5: Time: 3000 s / Temp.: 60°C End segment: ON / Vaccum : OFF Segment 6: Time: 2700 s / Temp.: 30 End Seg		3.3 hr	Place a single sheet of cleanroom paper under the substrates.
8.6	Relaxation delay	Wafer storage box			Overnight	
8.7	Development	Z13 / Wet Bench Solvent	PGMEA development in two separate baths		10 + 10 min	If a reaction is visible when you spray isopropanol (white residues appear), return to PGMEA. Repeat until isopropanol does not react with dissolved SU8 residues. Can rinse the wafer, dry and check the nozzles in the uscope.
8.8	Rinse	Z13 / Wet Bench Solvent	Isopropanol+Water		1 min, 30 s	Remember to rinse the wafer with water after isopropanol, then dry with n2 gun
8.9	Descum	Z11/ Tepla	Program 3		1 min	High, increase time if not enough
8.9	Inspection	Z13 / uScope	Check for residues, resolution and alignment			
				Time:	400 min	min without overnight
8	**DRIE 2 BACKSIDE**					
8.1	Si DRIE	Z2/Alcatel 601E	Si_ambiant2	180 um	~ 30 min	
8.2	Plasma O2 clean	Z2/Tepla GiGAbatch	O2 , 20 min, high		< 20 min	Watch graph to see when done
8.3	Inspection	Z6/uScope				
				Time:	60 min	
9	**PACKAGING**					
9.1	Dicing	Disco DAD321				

Appendix F

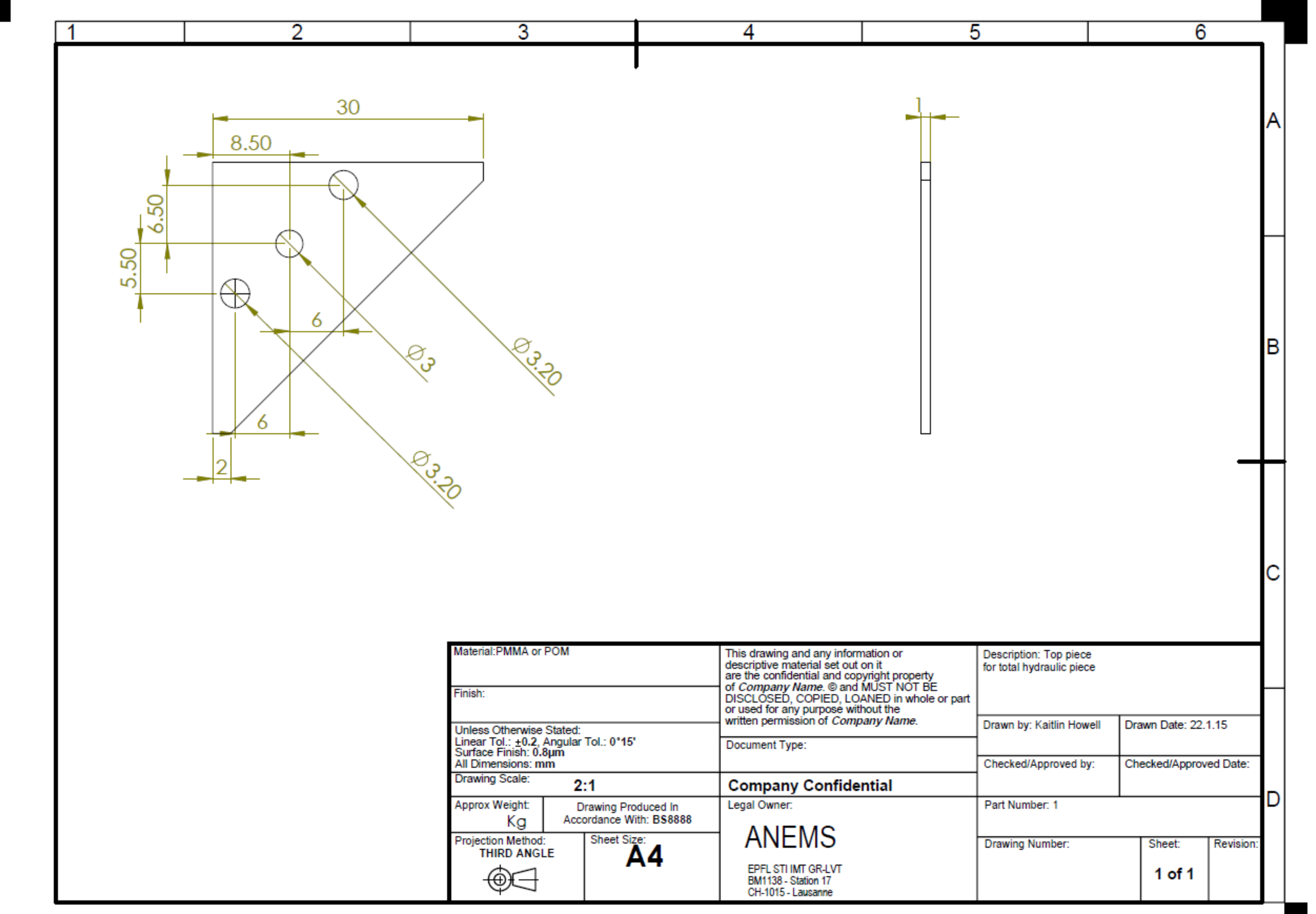

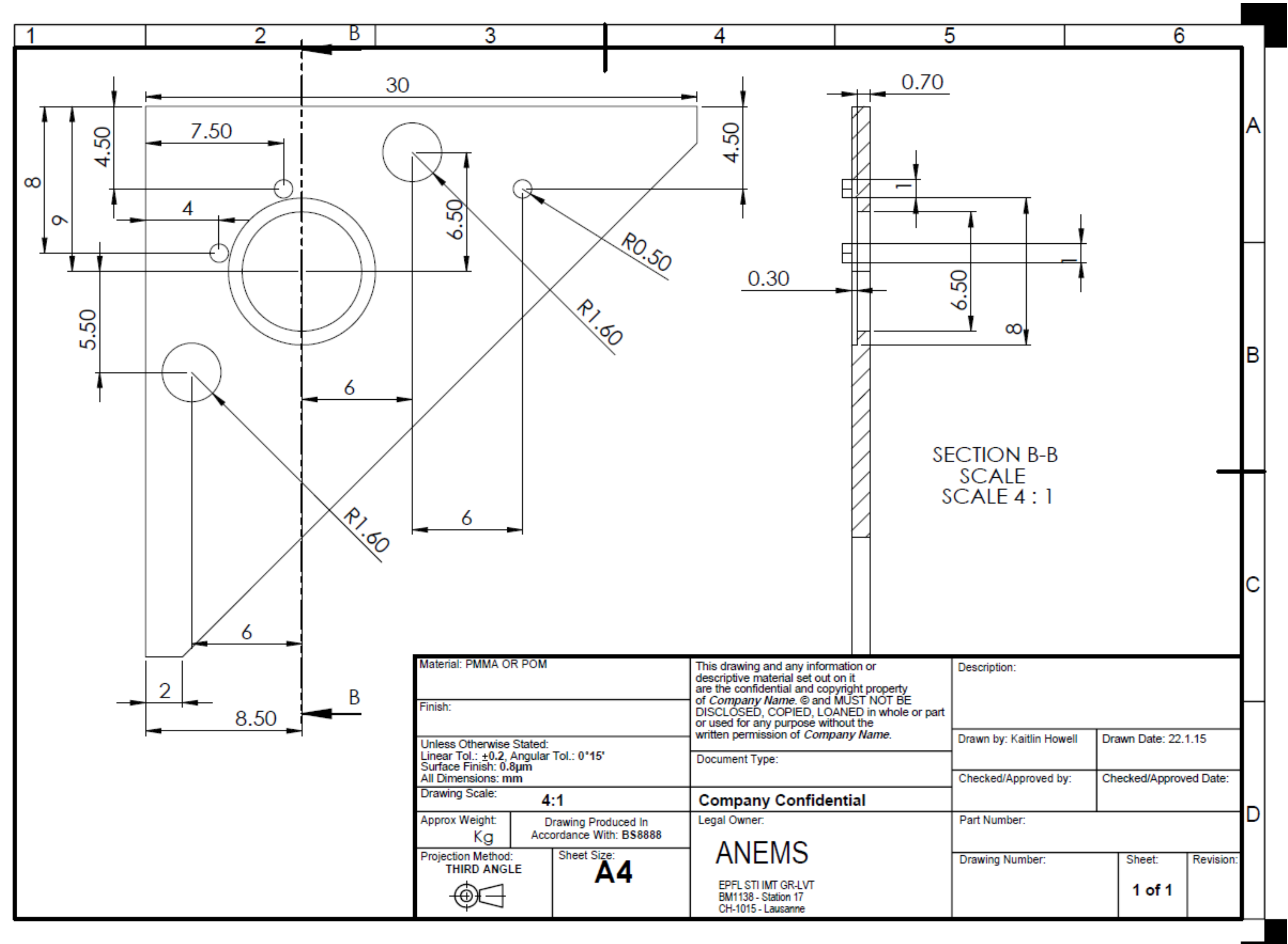
SECTION B-B
SCALE
SCALE 4 : 1
30
7.50
4.50
8
9
4
6.50
R0.50
R1.60
5.50
6
0.70
0.30
1
2
8.50
B
Material: PMMA OR POM
Finish:
Unless Otherwise Stated:
Linear Tol.: ±0.2, Angular Tol.: 0°15'
Surface Finish: 0.8µm
All Dimensions: mm
Drawing Scale: 4:1
Approx Weight: Kg
Drawing Produced In Accordance With: BS8888
Projection Method: THIRD ANGLE
Sheet Size: A4
This drawing and any information or descriptive material set out on it are the confidential and copyright property of Company Name. © and MUST NOT BE DISCLOSED, COPIED, LOANED in whole or part or used for any purpose without the written permission of Company Name.
Document Type:
Company Confidential
Legal Owner:
ANEMS
EPFL STI IMT GR-LVT
BM1138 - Station 17
CH-1015 - Lausanne
Description:
Drawn by: Kaitlin Howell
Drawn Date: 22.1.15
Checked/Approved by:
Checked/Approved Date:
Part Number:
Drawing Number:
Sheet: 1 of 1
Revision:

Appendix G

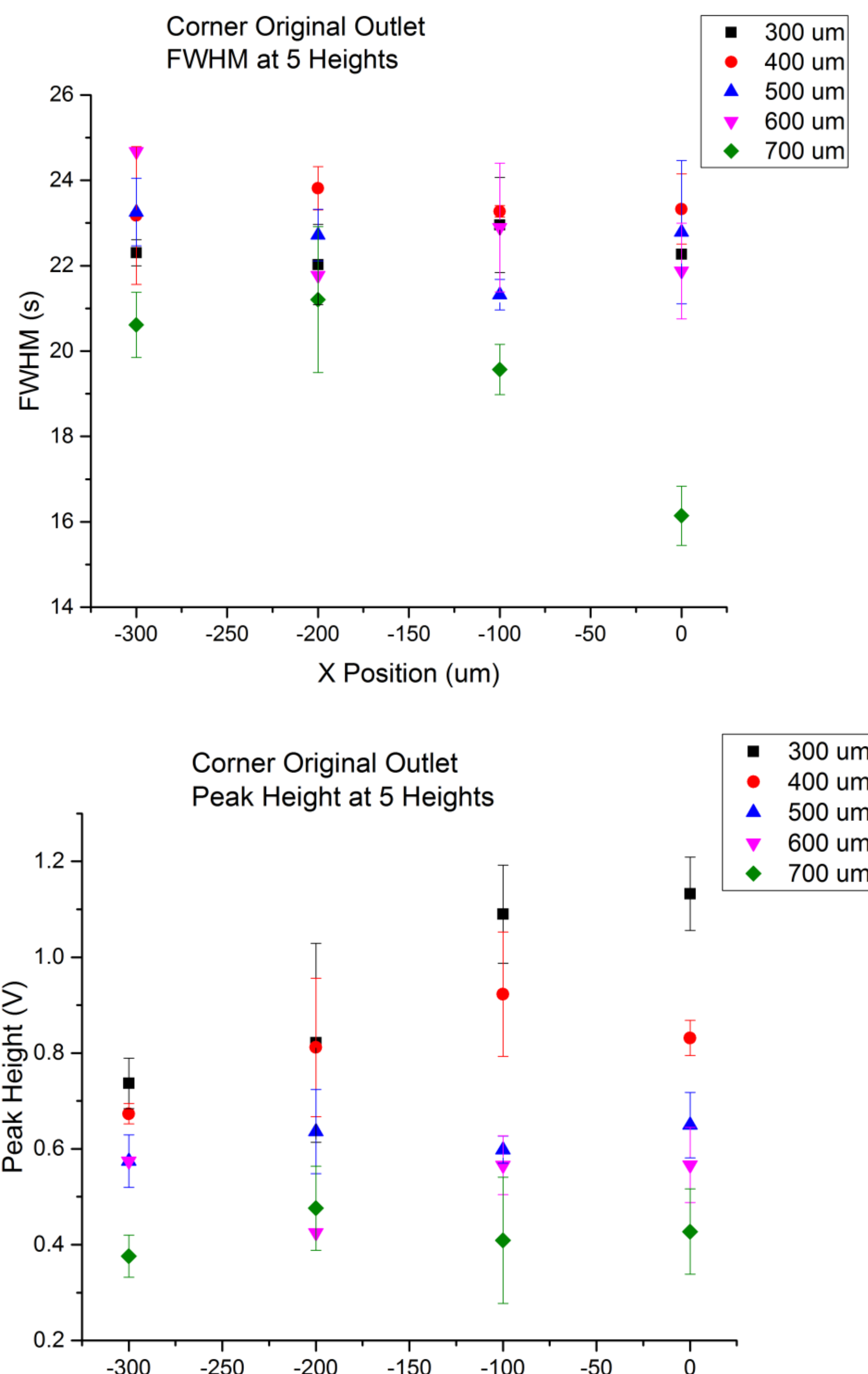

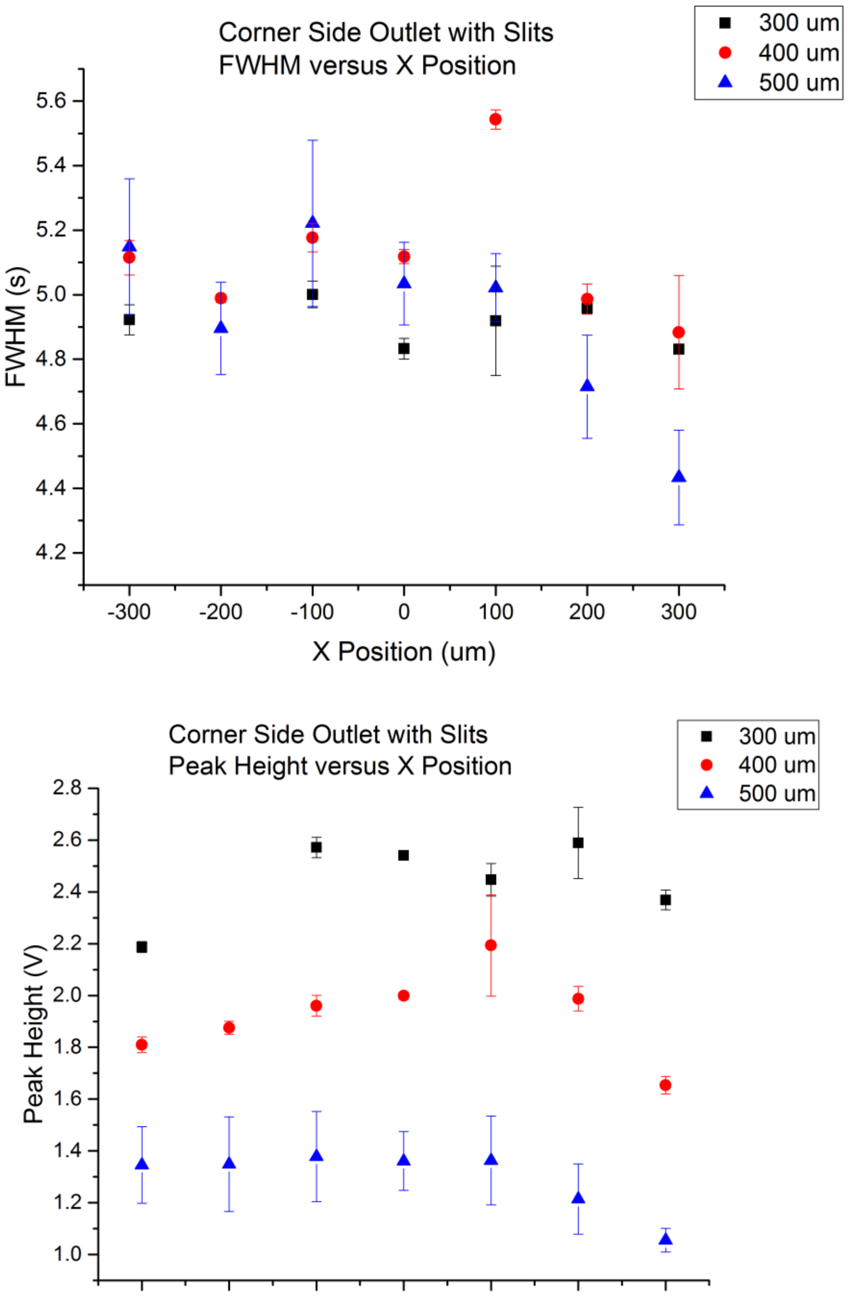
Corner Side Outlet with Slits
FWHM versus X Position
300 um
400 um
500 um
FWHM (s)
5.6
5.4
5.2
5.0
4.8
4.6
4.4
4.2
-300
-200
-100
0
100
200
300
X Position (um)
Corner Side Outlet with Slits
Peak Height versus X Position
300 um
400 um
500 um
Peak Height (V)
2.8
2.6
2.4
2.2
2.0
1.8
1.6
1.4
1.2
1.0
-300
-200
-100
0
100
200
300
X Position (um)